

# AIVP

## ADVANCES IN IMAGE AND VIDEO PROCESSING



## TABLE OF CONTENTS

EDITORIAL ADVISORY BOARD	I
DISCLAIMER	II
<b>Color Image Compression using hybrid Haar-DCT wavelet in Different color spaces</b> H. B. Kekre, Tanuja Sarode and Prachi Natu	1
<b>Method of Hardware Selection of Characteristic Features Based on Radon Transformation and not Sensitive to Rotation, Shifting and Scale of the Input Images</b> Stepan Bilan, Ruslan Motornyuk and Sergii Bilan	12
<b>Performance Improvement by Sorting the Transform Coefficients of Host and Watermark using Unitary Orthogonal Transforms Haar, Walsh and DCT</b> H. B. Kekre, Tanuja Sarode and Shachi Natu	24
<b>Study of Erosion Processes in the Tinto Salt-Marshes with Remote Sensing Images</b> Emilio Ramírez-Juidías	39
<b>A New Comparative Study of Radiometric Correction on Satellite Images Using Kalman Filter and Levenberg Marquardt Algorithm</b> Priti Tyagi and Udhav Bhosle	53

---

## **EDITORIAL ADVISORY BOARD**

**Dr Zezhi Chen**

Faculty of Science, Engineering and Computing; Kingston University London  
*United Kingdom*

**Professor Don Liu**

College of Engineering and Science, Louisiana Tech University, Ruston,  
United States

**Dr Lei Cao**

Department of Electrical Engineering, University of Mississippi,  
United States

**Professor Simon X. Yang**

Advanced Robotics & Intelligent Systems (ARIS) Laboratory, University of Guelph,  
Canada

**Dr Luis Rodolfo Garcia**

College of Science and Engineering, Texas A&M University, Corpus Christi  
United States

**Dr Kyriakos G Vamvoudakis**

Dept of Electrical and Computer Engineering, University of California Santa Barbara  
United States

**Professor Nicoladie Tam**

University of North Texas, Denton, Texas  
United States

**Professor Shahram Latifi**

Dept. of Electrical & Computer Engineering University of Nevada, Las Vegas  
United States

**Professor Hong Zhou**

Department of Applied Mathematics Naval Postgraduate School Monterey, CA  
United States

**Dr Yuriy Polyakov**

Computer Science Department, New Jersey Institute of Technology, Newark  
United States

**Dr M. M. Faraz**

Faculty of Science Engineering and Computing, Kingston University London  
United Kingdom

---

## **DISCLAIMER**

All the contributions are published in good faith and intentions to promote and encourage research activities around the globe. The contributions are property of their respective authors/owners and the journal is not responsible for any content that hurts someone's views or feelings etc.

# Color Image Compression using hybrid HAAR-DCT wavelet in Different color spaces

H. B. Kekre<sup>1</sup>, Tanuja Sarode<sup>2</sup>, Prachi Natu<sup>3</sup>

<sup>1,3</sup>MPSTME, NMIMS University, Mumbai, India;

<sup>2</sup>TSEC, Mumbai University, India;

hbkekre@yahoo.com, tanuja\_0123@yahoo.com, prachi.natu@yahoo.com

## ABSTRACT

This paper compares digital image compression in various color spaces using Hybrid Haar wavelet transform. As DCT has high energy compaction property, it is combined with Haar transform generating Haar-DCT hybrid wavelet transform. Different component sizes are used and error at different compression ratios up to 32 is observed. At higher compression ratios 16-16 component pair gives minimum error. This pair is further used to compress images in different color spaces like RGB, KLUV, YUV, YIQ, XYZ and YCbCr. KLUV color space show considerably less Root Mean Square Error (RMSE) and Mean Absolute Error (MAE) than other color spaces. Average Fractional Change in Pixel Value (AFCPV) in KLUV color space is nearly half than other color spaces. RMSE, MAE these measures are not sufficient as it give perceived error to human visual system. Hence other error metric Structural Similarity Index (SSIM) is used to observe performance superiority of various color spaces. SSIM in KLUV and RGB color space is equal having value 0.994 which is closest to one indicating better but similar image quality in both color spaces. This observation cannot be emphasized using traditional error metrics like RMSE, MAE and AFCPV.

**Keywords:** Image Compression, Hybrid Wavelet Transform, SSIM, AFCPV

## 1 Introduction

Digital images are integral part of multimedia data and used extensively in many applications today. Also large amount of image data is transferred over internet. To facilitate easy storage and reduction in bandwidth required to transmit this data, compression of data becomes necessary. Compression reduces the number of bits required to represent an image. Data is compressed before storage and transmission and at the receiving end it is decompressed to get original data back. If decompressed data does not show any loss of contents then it is called as lossless compression. In contrast to this if decompressed data is different than original data it means that some loss of information is there and such type of compression is called as lossy

compression. Lossy compression gives higher compression ratio than lossless compression. In image compression loss of redundant information not visible to human visual system is acceptable. Hence lossy compression is preferred for images.

Many transform based image compression methods are available in literature. Still in last two decades use of wavelets is emphasized for image compression. Wavelet transform gives time and frequency analysis of a signal. It is good in time resolution of high frequencies, while for slowly varying functions, it is good in frequency resolution. Basic idea behind wavelet is to select function prototype called mother wavelet. Then scaled and shifted version of mother wavelet can be used to analyze the image data. Due to high energy compaction property, it gives better compression ratio than Fourier Transform, Short Term Fourier Transform (STFT) [1] and popularly used Discrete Cosine Transform (DCT) [2]. Multi-resolution analysis [3] is another important property of wavelet transform that helps to view the signal at different levels. Aim of this paper is to use hybrid wavelet transform for color image compression in different color spaces.

## 2 Review of Literature

Image compression using wavelet transform is focused by many researchers since last two decades. M. S. Abdullah and N. Subba Rao [4] have proposed comparison of different wavelets for image compression. Daubechies wavelet [5], Haar wavelet, Coiflet, Symlet and bi orthogonal Wavelet transforms have been used to compare their performances. Wei Pin Lin et al. proposed a method [6] to predict the data of high frequency from a decimated image with specified down sampling rule. It exploits the correlation between low pass and high pass outputs which can be used to compress the image and get good quality reconstructed image. Tree based wavelet image coder is proposed by Jose Oliver, Manuel P. Malumbres [7]. In this method wavelet tree is formed by logically arranging transform coefficients so as to remove the redundancy among the sub bands. Arian Maleki et al. have proposed image compression using directional wavelet transforms [8]. To avoid the drawback of quad tree partitioning, they have used new scheme of partitioning called mega quad partitioning. Shih-Chung B. Lo, Huai Li, and Matthew T. Freedman have proposed neural network based wavelet transform for image compression [9]. They have used linear convolution neural network to seek the wavelet that minimizes the error and maximizes the efficiency. Daubechies wavelet and Haar wavelet have been used by them for compression. A hybrid image compression technique implementing a four-dimensional transform combining the discrete wavelet transform and the discrete cosine transform has been proposed by E. Elharar et al. [10]. It is used for integral imaging and outperforms JPEG compression scheme applied to integral images. Image compression using dual tree complex wavelet transform is presented by Li Hui Fang et al. [11]. It uses SPIHT algorithms, which is based on not only the relationship between the bit-planes and the target bit-rate but also the relationship between the initial threshold and the target bit-rate. Combination of fractal image

encoding and wavelet decomposition is proposed in by Xiao-Yan Xu et al. [12]. In their proposed process of encoding, the image is dealt by three level wavelet decomposition. High frequency section of the decomposed image adopts scathless predicting encoding, while the low frequency section adopts fractal compression encoding. In the process of decoding, the high frequency section carries out scathe less predicting decoding, while the low frequency section is decoded to iterative function system code which is used for subimage reconstruction. Compression using hybrid transform is presented in [13]. Kronecker product of Kekre transform with other orthogonal transforms is used and error at different compression ratios is observed. It has been observed that when DCT is combined with Kekre transform gives minimum error as DCT has high energy compaction property than other orthogonal transforms.

Simple wavelet generation method proposed by Kekre et al. [14] is used to compare performance of wavelet transforms to respective orthogonal transforms [15]. It has been observed that wavelet transforms of orthogonal transforms give better compression than respective orthogonal transform. Next advancement to wavelet transforms is hybrid wavelet transform that uses two different orthogonal transforms to generate new transformation matrix. In recent years hybrid wavelet transforms have been studied and proven to be better than wavelet transform in many image processing applications including image compression. Compression using Real Fourier-DCT hybrid wavelet transform is proposed by Kekre et al. [16]. It shows that when RealDFT and DCT are combined to generate hybrid wavelet, it gives better performance than compression obtained by individual DCT or Real DFT. It is also better than DCT wavelet transform [8]. Hybrid wavelet of Haar and non sinusoidal transforms has been proposed in [17]. Different sizes of component transforms have been tried and one giving better image quality has been selected. On the other hand Haar transform paired with sinusoidal transforms is used for image compression [18]. Haar transform paired with DCT gives superior performance than its combination with DST, Hartley and Real-DFT.

This paper is extension of our previous work based on hybrid Haar wavelet transform. Here Haar-DCT hybrid wavelet is used for compressing images in various color spaces. Different error metrics are used as RMSE is not a substantial measure to observe the performance in different color spaces.

### 3 Proposed Method

Let  $A$  denotes  $M \times M$  base component transform and  $B$  denotes  $N \times N$  local component transform. Then using  $A$  and  $B$  hybrid wavelet  $T$  of  $MN \times MN$  size is generated using Kekre's algorithm. First ' $M$ ' rows of resultant matrix are calculated by repeating each column of ' $A$ ', ' $N$ ' times and multiplying it with each element of first row of  $B$ . These ' $M$ ' rows represent global characteristics in hybrid wavelet transform. Remaining rows are obtained by translating the rows of matrix  $B$  and padding zeroes to it from second row onwards. These rows contribute local features of an image. Generated hybrid wavelet transform is shown below in Figure 1.

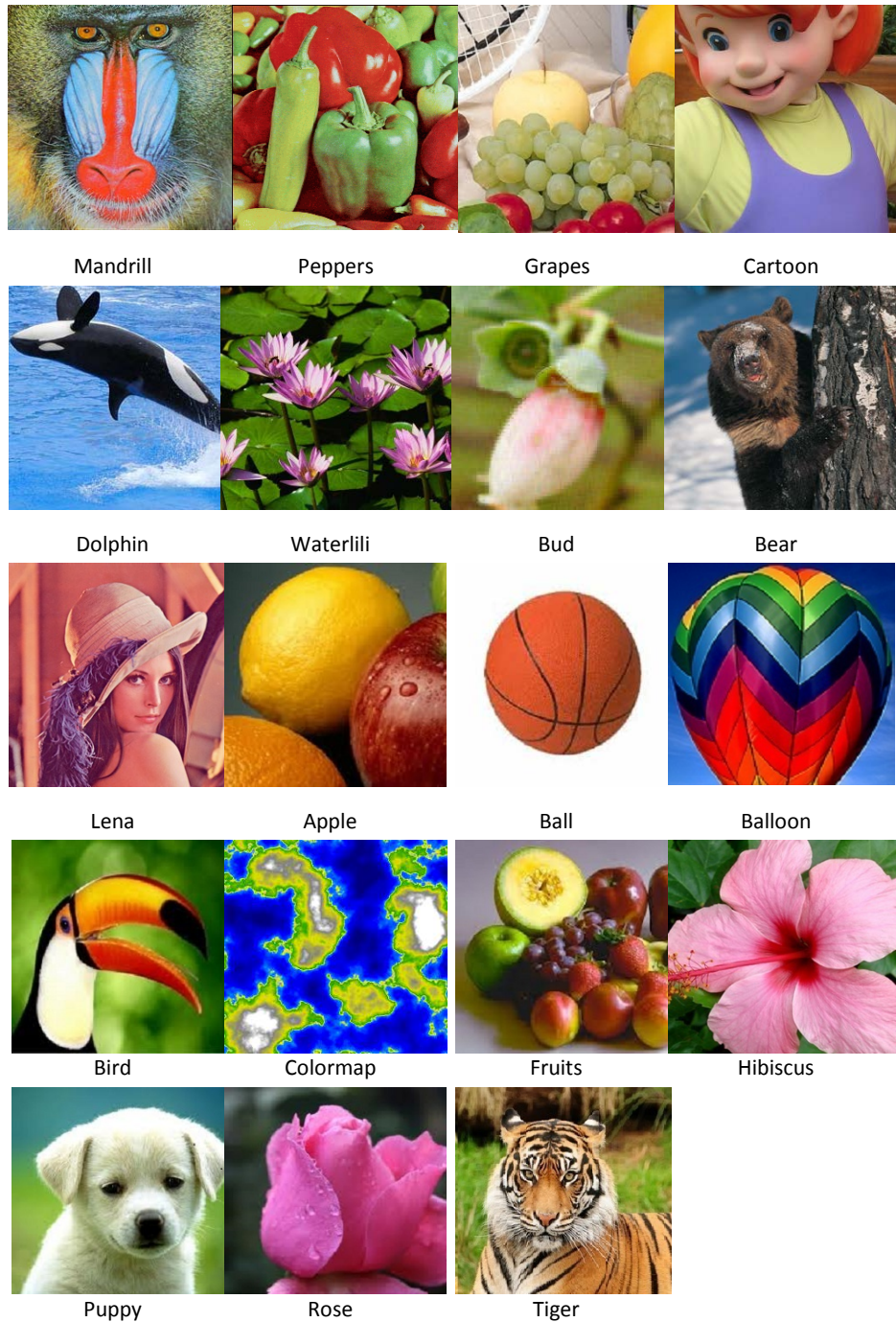
$\begin{pmatrix} a_{11} \\ a_{21} \\ \vdots \\ \vdots \end{pmatrix}$	...	$\begin{pmatrix} a_{11} \\ a_{21} \\ \vdots \\ \vdots \end{pmatrix}$	$\begin{pmatrix} a_{12} \\ a_{22} \\ \vdots \\ \vdots \end{pmatrix}$	...	$\begin{pmatrix} a_1 \\ a_2 \\ \vdots \\ a_2 \end{pmatrix}$	.....	$\begin{pmatrix} a_{1m} \\ a_{2m} \\ \vdots \\ \vdots \end{pmatrix}$	.....	$\begin{pmatrix} a_{1m} \\ a_{2m} \\ \vdots \\ \vdots \end{pmatrix}$
$b_{21}$	...	$b_{2n}$	0	0	0	.....	0	...	0
0	0	0	$b_{21}$	...	$b_{2n}$	.....	0	...	0
.	.	.	.	.	.	.....	.	.	.
.	.	.	.	.	.	.	.	.	.
0	0	0	0	0	0	.	$b_{21}$	...	$b_{2n}$
$b_{31}$	...	$b_{3n}$	0	0	0	.	0	...	0
0	0	0	$b_{31}$	...	$b_{3n}$	.	0	...	0
.	.	.	.	.	.	.	.	.	.
.	.	.	.	.	.	.	.	.	.
0	0	0	0	0	0	.	$b_{31}$	...	$b_{3n}$
.	.	.	.	.	.	.	.	.	.
.	.	.	.	.	.	.	.	.	.
$b_{n1}$	...	$b_{nn}$	0	0	0	.	0	0	0
0	0	0	$b_{n1}$	...	$b_{nn}$	.	0	0	0
.	.	.	.	.	.	.	.	.	.
.	.	.	.	.	.	.	.	.	.
0	0	0	0	0	0	.	$b_{n1}$	...	$b_{nn}$

Figure 1: Generation of Hybrid Wavelet Matrix using Component Matrices A and B

Hybrid wavelet using different component size is generated and applied on images. To generate 256x256 size transformation matrix, different component sizes used are 8-32, 16-16, 32-8 and 64-4. Here 8-32 means 8x8 base transform and 32x32 local transform. Here Haar transform is used as base transform and DCT is used as local component transform to generate Haar-DCT hybrid wavelet of size 256x256.

## 4 Results and Discussions

Proposed method is applied on a set of color images belonging to different classes. Each image is of size 256x256. Execution is done on AMD dual core processor using Matlab 2012. Set of test images is shown in Figure 2.



**Figure 2: Test Set of Images from Different Classes**

Figure 3 shows graph of RMSE versus compression ratio for Haar-DCT hybrid wavelet transform. To obtain transformation matrix of size 256x256, different component sizes like 8x8 Haar and 32x32 DCT can be selected. It is denoted as 8-32 for reading simplicity. Similarly 16-16, 32-8 and 64-4 pairs can also be used.

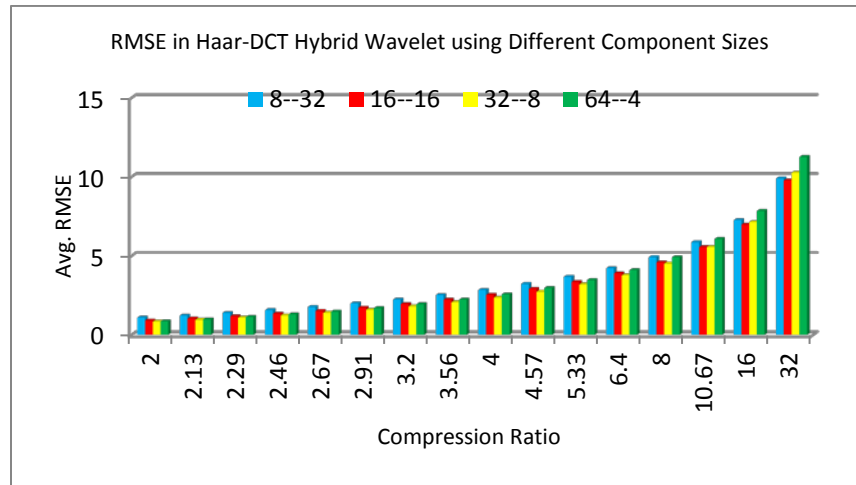


Figure 3: RMSE in Haar-DCT Hybrid Wavelet Transform With Variation in Component Sizes

It has been observed that for lower compression ratios up to 8, a pair that gives less RMSE is 32-8. At compression ratio 10.67, both pairs of 16-16 and 32-8 give equal error and at higher compression ratios 16-16 component size give less error.

This combination is further used to compress image in different color spaces. Six different color spaces namely RGB, KLUV, XYZ, YUV, YIQ, YCbCr have been used. RMSE against compression ratio in these different color spaces is plotted in fig. 4.

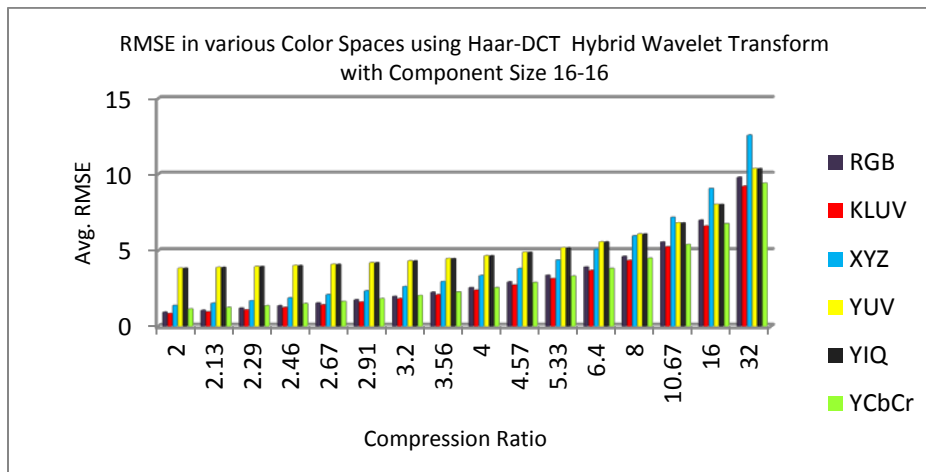


Figure 4: RMSE in various Color Spaces using Haar-DCT Hybrid Wavelet Transform with Component Size 16-16

From Figure 4 it has been observed that, RMSE obtained in KLUV color space is less than RMSE in other color spaces for all compression ratios. Error in YCbCr color space is slightly more than in KLUV color space and it is followed by error in RGB color space. XYZ color space shows maximum error. YIQ and YUV color space show same error.

Further mean absolute difference between original image and reconstructed image is computed. In Figure 5, MAE at various compression ratios is plotted for different color spaces.

Error pattern obtained is similar to that of RMSE. Lowest MAE is obtained in KLUV color space followed by MAE in YCbCr color space and then RGB color space.

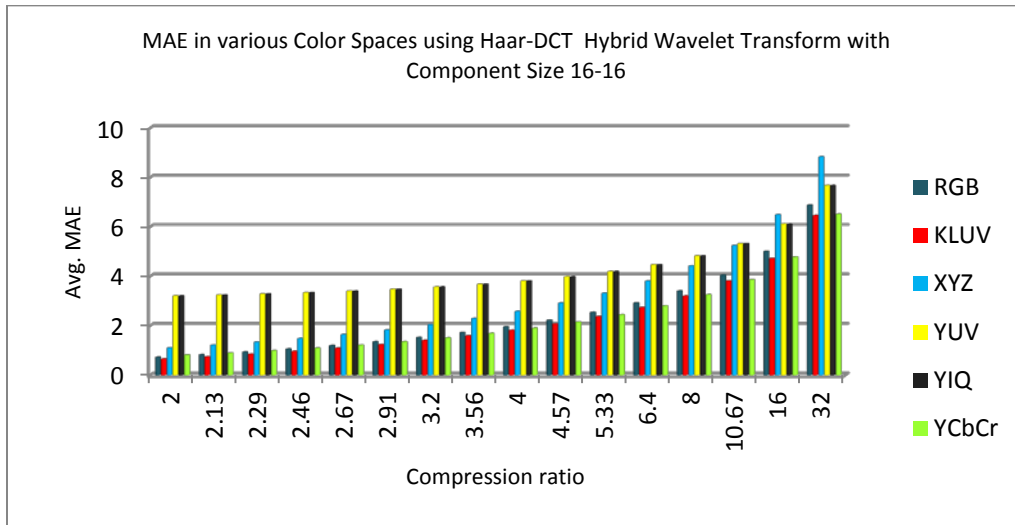


Figure 5: MAE in various Color Spaces using Haar-DCT Hybrid Wavelet Transform with Component Size 16-16

AFCPV for various color spaces is plotted in Figure 6. In KLUV color space AFCPV is nearly half of AFCPV obtained in RGB, XYZ, YUV and YIQ color spaces.

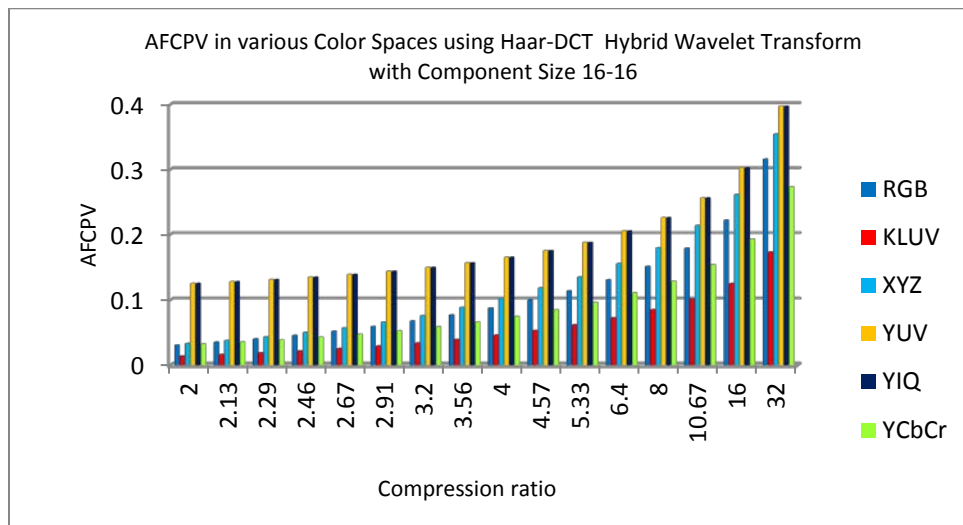
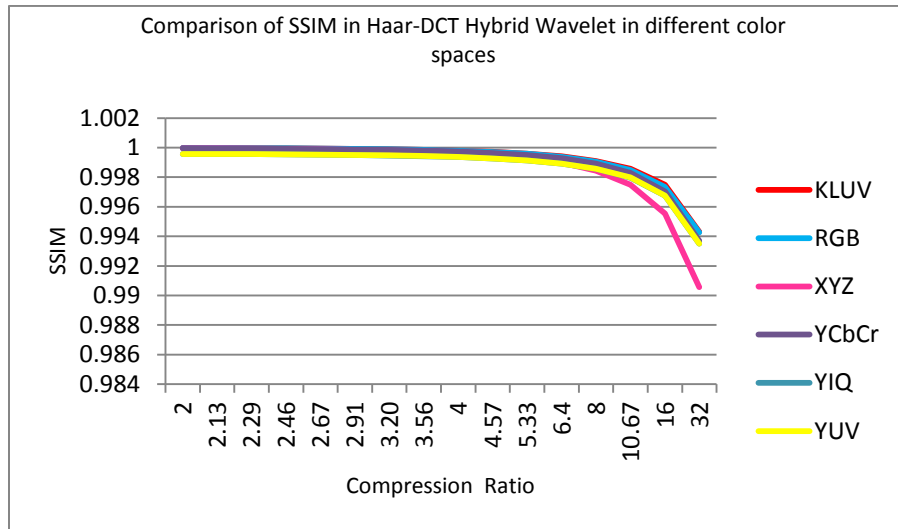


Figure 6: AFCPV in various Color Spaces using Haar-DCT Hybrid Wavelet Transform with Component Size 16-16

Figure 7 shows SSIM plotted against compression ratio. SSIM considers image degradation as perceived change in structural information. Hence provides good approximation to perceived image quality. Value of SSIM ranges between -1 to 1. It is 1 for exactly similar images.



**Figure 7: Comparison of SSIM in Haar-DCT Hybrid Wavelet in different color spaces**

As shown in Figure 7, SSIM in KLUV color space at compression ratio 32 is 0.9943. It indicates that reconstructed image quality is closer to original image. In RGB color space SSIM value is equal to 0.994 showing similar image quality. SSIM measure in YUV, YIQ and YCbCr color space exhibit similar performance showing value 0.993. XYZ color space shows lowest SSIM means that lower image quality.

Figure 8 shows reconstructed image ‘Lena’ obtained using Haar-DCT hybrid wavelet transform at compression ratios 4, 8, 16 and 32 respectively. Different color spaces used are RGB, YCbCr, XYZ, KLUV, YIQ and YUV. SSIM value of each image is indicated below the image. From figure it is clear that, SSIM value closest to 1 indicates that reconstructed image with better quality is obtained. With increase in compression ratio SSIM value decreases. Though similar AFPCV values are obtained at specific compression ratio, difference in reconstructed image quality is highlighted by SSIM values of image at that compression ratio.

Color space	Compression Ratio			
	4	8	16	32
RGB				
SSIM	1	0.999	0.997	0.994
AFPCV	0.021	0.041	0.066	0.097

YCbCr					
	SSIM	0.999	0.998	0.997	0.993
	AFCPV	0.020	0.039	0.064	0.097
XYZ					
	SSIM	0.999	0.998	0.995	0.990
	AFCPV	0.018	0.039	0.065	0.097
KLUV					
	SSIM	1	0.999	0.998	0.9943
	AFCPV	0.006	0.011	0.019	0.028
YIQ					
	SSIM	0.999	0.998	0.996	0.993
	AFCPV	0.035	0.051	0.075	0.106
YUV					
	SSIM	0.999	0.998	0.996	0.993
	AFCPV	0.035	0.051	0.075	0.106

Figure 8: Reconstructed 'Lena' Image in Various Color Spaces using Haar-DCT hybrid Wavelet Transform at Different Compression Ratios

## 5 Conclusion

In this paper performance of Haar-DCT hybrid wavelet in various color spaces is compared. From different component size combinations, 16-16 component size is observed to better in

RGB color space and is used in different color spaces. Different error metrics are used to compare the performance as RMSE gives the information about the perceived error. KLUV color space shows minimum error than other color spaces in terms of RMSE, MAE and AFCPV. Compression in KLUV color space can be better measured in terms of SSIM than RMSE, MAE and AFCPV in any color space. SSIM of 0.9943 is obtained in KLUV color space at compression ratio 32. As it is closest to 1 it indicates that reconstructed image is much similar to original image. It is closely followed by RGB color space showing slight less SSIM than KLUV color space. Though RMSE, MAE and AFCPV in KLUV color space is considerably less than respective values in RGB color space, SSIM values show negligible difference in these two color spaces. It indicates slight difference in quality of reconstructed images

### REFERENCES

- [1]. Strang G. "Wavelet Transforms Versus Fourier Transforms." *Bull. Amer. Math. Soc.* 28, 1993, 288-305.
- [2]. N. Ahmed, T. Natarajan and K. R. Rao, "Discrete Cosine Transform", *IEEE Transaction Computers*, January 1974, C-23, pp. 90-93.
- [3]. S. Mallat, "A Theory of Multiresolution Signal Decomposition: The Wavelet Representation," *IEEE Trans. Pattern Analysis and Machine Intelligence*, vol. 11, pp. 674-693, 1989.
- [4]. M.S. Abdullah, N. Subba Rao, "Image Compression using Classical and Lifting based Wavelets", *International Journal of Advanced Research in Computer and Communication Engineering*, August 2013, Vol. 2, Issue 8, pp. 3193-3198.
- [5]. Daubechies, I. "The wavelet transform, time-frequency localization and Signal analysis", *IEEE Transformation and Information Theory* 36: 1990, 961-1005.
- [6]. Wei-Pin Lin, Chih-Ming Chen, and Yung-Chang Chen, "Image Compression with Interpolation in Wavelet Transform Domain" 2005. *IEEE International Symposium on Circuits and Systems (ISCAS)*, 2005, Vol. 3, pp. 2084 – 2087.
- [7]. Jose Oliver, Manuel P. Malumbres, "Low Complexity Multi-Resolution Image Compression using Wavelet Lower Trees", *IEEE Trans. on Circuits and Systems for Video Technology*, Nov. 2006, Vol. 16, Issue 11, pp. 1437-1444.
- [8]. Maleki A, Rajaei B, Pourreza H.R., "Rate Distortion Analysis of Directional Wavelets", *IEEE Trans. on Image Processing*, Feb 2012, Vol. 21 Issue 2, pp. 588-600.
- [9]. Shih-Chung B. Lo, Huai Li, and Matthew T. Freedman, "Optimization of Wavelet Decomposition for Image Compression and Feature Preservation", *IEEE Trans. on Medical Imaging*, Vol. 22, Issue 9, Sept 2013, pp. 1141-1151.

- [10]. E. Elharar, Adrian Stern, Ofer Hadar, and Bahram Javidi, "A Hybrid Compression Method for Integral Images using Discrete Wavelet Transform and Discrete Cosine Transform", *Journal Of Display Technology*, September 2007, Vol. 3, No. 3, pp. 321-325.
- [11]. Jingyu Yang, Wenli Xu, Qionghai Dai, Yao Wang, "Image Compression using 2D Dual Tree Discrete Wavelet Transform (DDWT)", *IEEE International Symposium on Circuits and Systems*, May 2007, pp. 297-300.
- [12]. Xiao-Yan Xu, Chen, P., Juan Dai, "Hybrid Encoding Analysis of Fractal Image Compression Method Based on Wavelet Transform", In *Proc of International Conference of Machine Learning and Cybernetics*, 2008, Vol. 5, pp. 2886-2889.
- [13]. H.B. Kekre, Tanuja Sarode, Prachi Natu, "Digital Image Compression using Hybrid Transform with Kekre Transform and Other Orthogonal Transforms", *Journal of Computer Engineering*, Jan. 2014, Vol. 16, Issue 1, Ver. III, PP 38-46.
- [14]. H. B. Kekre, Tanuja Sarode, Sudeep Thepade, Sonal Shroff, "Instigation of Orthogonal Wavelet Transforms using Walsh, Cosine, Hartley, Kekre Transforms and their use in Image Compression", *International Journal of Computer Science and Information Security*, 2011, Vol. 9, No. 6, pp. 125-133.
- [15]. H.B. Kekre, Tanuja Sarode, Prachi Natu, " Image Compression Using Column, Row and Full Wavelet Transforms Of Walsh, Cosine, Haar, Kekre, Slant and Sine and Their Comparison with Corresponding Orthogonal Transforms". *International Journal of Engineering Research and Development (IJERD)*, Mar.2013, Vol. 6. Issue 4, pp. 102-113.
- [16]. H.B. Kekre, Tanuja Sarode, Prachi Natu, "Image Compression using Real Fourier Transform, It's Wavelet Transform and Hybrid Wavelet with DCT", *International Journal of Advanced Computer Science and Applications (IJACSA)*, 2013, Vol. 4, No.5, pp. 41-47.
- [17]. H.B. Kekre, Tanuja Sarode, Prachi Natu, "Color Image Compression using Hybrid Wavelet Transform with Haar as Base Transform", *International Journal of Scientific and Research Publications*, June 2014, Volume 4, Issue 6, pp. 1-13.
- [18]. H.B. Kekre, Tanuja Sarode, Prachi Natu, "Performance Comparison of Hybrid Haar Wavelet Transform with Various Local Transforms in Image Compression using Different Error Metrics", *International Journal of Image Processing (IJIP)*, July 2014, Vol.8, Issue 4, pp. 186-203

# Method of Hardware Selection of Characteristic Features Based on Radon Transformation and not Sensitive to Rotation, Shifting and Scale of the Input Images

Stepan Bilan<sup>1</sup>, Ruslan Motornyuk<sup>2</sup>, Sergii Bilan<sup>3</sup>

<sup>1</sup>Faculty "Infrastructure and rolling stock of railways", State Economy and Technology University of Transport, Kiev, Ukraine

<sup>2</sup>Data Processing Center of Southwestern Railways, Kyiv, Ukraine

<sup>3</sup>Win-Interactive LLC, Vinnytsia, Ukraine

<sup>1</sup>bstepan@ukr.net, <sup>2</sup>xehap0@gmail.com, <sup>3</sup>belan@svitonline.com

## ABSTRACT

In this paper considered by the method of the organization of cellular automata to extract characteristic features of images based on the Radon transform. Cellular automata are constructed using a hexagonal surface. This increases the efficiency of image recognition. This made it possible to implement the Radon transform on the six directions. This cellular automata was simulated in the software environment of Active-HDL, and also was created his software model. Experimental studies for both models showed high results of recognition for the different levels of noise that are present in the image.

**Keywords:** Cellular automata, Radon transform, Image recognition, Hexagonal coverage.

## 1 Introduction

In 1917, the mathematician J. Radon [1,2] proposed a method of renewal (reconstruction) of multidimensional functions by their integral characteristics. The method solves the inverse problem of integral geometry. Besides of the main applications of the Radon transform (RT) (computed tomography [3,4], seismology) there are papers which prove its effectiveness on the allocation of characteristic features such as image recognition tasks [5] and at the analysis of their structure [1,5–9].

On the basis of RT we can build a system for automatic recognition of visual images. Shortcomings in the existing fields of application are:

- 1) - medical tomographs implement this method through hardware, though relatively quickly, but not used for image of task recognition;

- 2) – with digital imaging the entire volume calculations of Radon transform (which has a direct relationship with the Fourier transform [3], and hence a similar computational complexity), falls on CPU, which can not provide the performance for real-time.

Medical tomographs are stationary bulky devices that can not be effectively used anywhere, especially for the problem of recognition.

In this paper we consider the possibility of combining of hardware implementation of projections RT with small size of device. Hexagonal cells is used for organization of cellular automaton (CA), which provides high accuracy in image recognition and speed comparable to that of real-time [10–17]. RT is considered in six directions through the implementation of CA, based on cells with a hexagonal shape.

## 2 Implementation of RT model on the CA with a hexagonal coated

In [3] it is determined that a sufficient minimum number of RT projections, which is possible to restore primary image is three: the directions  $0^\circ$ ,  $60^\circ$  and  $120^\circ$ . Hence a set of three projections can be regarded as the characteristic feature that is already possible to perform image recognition. But the above-mentioned angles ( $0^\circ$ ,  $60^\circ$  and  $120^\circ$ ) exactly coincide with the directions of the hexagonal coverage (fig. 1,a) [15,17]. Moreover, the hexagonal lattice is possible to allocate not only 3 but and 6 lines (fig. 1,b). As shown in Figure 1,a is a cellular automaton in the form of a regular hexagon shape repeats its view of the hexagonal unit pixel. The same figure shows the lines of the main directions of the hexagonal coverage - is  $0^\circ$ ,  $60^\circ$  and  $120^\circ$ . Besides the main directions of hexagonal raster has additional directions corresponding corners  $30^\circ$ ,  $90^\circ$  and  $150^\circ$ . All these directions and their relative positions are shown in Figure 1,b, hence it is in these areas hexagonal raster enables constructing six projections RT (fig. 1,b). Hence, if you imagine the processed image as a homogeneous structure or matrix having a hexagonal surface (Fig. 1,a) and give it some rules of functioning, you can get a result in the form of six projections on directions RT  $0^\circ$ ,  $30^\circ$ ,  $60^\circ$ ,  $90^\circ$ ,  $120^\circ$ ,  $150^\circ$  (fig. 1,b).

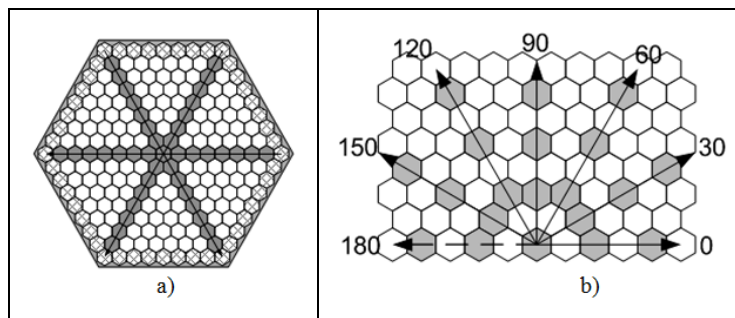


Figure 1: «Congenital» directions of hexagonal coverage

Such homogeneous structures have long been invented and are called CA. The main interest of the specialists in the field of computer science to cellular automata is caused by the fact that

they form a parallel computing paradigm, just as Turing machine paradigm successive forms. Thus, they can be used as models which own natural parallelism [10–18].

Consider the Radon transform and its physical content in more detail.

The most important practical and at the same time the simplest case is a function of two variables.

Suppose we are given a function  $f(x,y)$ , which is defined on some interval  $D$  [3,4]. Consider in the plane  $xy$  the line  $L$ , which intersect area  $D$  (fig. 2). Then, by integrating the function  $f(x, y)$  along the line  $L$ , we obtain the projection or linear integral of functions  $f$ . Integration along all possible lines  $L$  allows to define the RT for the function  $f(x,y)$ :

$$\check{f} = Rf = \int_L f(x, y) ds \quad (1)$$

where  $ds$  — increment of length along the line  $L$ .

As is known [1-3] RT function  $f(x, y)$  for the two-dimensional case through the normal equation of the line  $L$  can be represented by a formula (fig. 2):

$$\check{f}(p, \varphi) = Rf = \int_{-\infty}^{\infty} f(p \cos \varphi - s \sin \varphi, p \sin \varphi + s \cos \varphi) ds \quad (2)$$

where  $p$  - distance from the origin to the line (fig. 2);

$\varphi$  – the angle between the  $p$  and  $x$ .

$ds$  - length of increment along the line  $L$ .

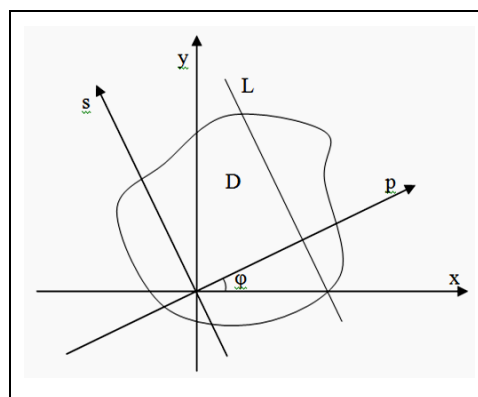


**Figure 2: Radon transform**

In a cellular automaton with a hexagonal surface (CAHS), which is built by hardware of six projections (sinograms) RT for directions  $0^\circ$ ,  $30^\circ$ ,  $60^\circ$ ,  $90^\circ$ ,  $120^\circ$  and  $150^\circ$  particular cases of the formula (2) will have the form:

For direction  $0^\circ$ :

$$f_0^v(p,0) = R_0 f = \int_{-\infty}^{\infty} f(p,s) ds$$

For direction 30°:

$$f_{30}^v(p,30) = R_{30} f = \int_{-\infty}^{\infty} f\left(\frac{\sqrt{3}}{2}p - \frac{1}{2}s, \frac{1}{2}p + \frac{\sqrt{3}}{2}s\right) ds$$

For direction 60°:

$$f_{60}^v(p,60) = R_{60} f = \int_{-\infty}^{\infty} f\left(\frac{1}{2}p - \frac{\sqrt{3}}{2}s, \frac{\sqrt{3}}{2}p + \frac{1}{2}s\right) ds$$

For direction 90°:

$$f_{90}^v(p,90) = R_{90} f = \int_{-\infty}^{\infty} f(s,p) ds$$

For direction 120°:

$$f_{120}^v(p,120) = R_{120} f = \int_{-\infty}^{\infty} f\left(-\frac{1}{2}p - \frac{\sqrt{3}}{2}s, \frac{\sqrt{3}}{2}p - \frac{1}{2}s\right) ds$$

For direction 150°:

$$f_{150}^v(p,150) = R_{150} f = \int_{-\infty}^{\infty} f\left(-\frac{\sqrt{3}}{2}p - \frac{1}{2}s, \frac{1}{2}p - \frac{\sqrt{3}}{2}s\right) ds$$

If necessary, a larger number of projections RT, which is allocated by hardware, can be used by two or more CAHS which are rotated relative to each other by an angle  $\beta$  to axis perpendicular to their plane:

$$\angle\beta = 30/n, \quad (3)$$

where  $n$  – is CAHS number, each of which performs a selection of RT by 6 directions.

Physical content of RT consists of finding of the sum of the brightness values of pixels, which forming this image, along a straight line in a certain direction. The results of these transformations will be arrays of values, which will transform the projections in the relevant directions.

Now we use the physical is content of the RT for set rules of operation of CA. To construct the projection sufficient to perform shift of the entire image in the desired direction. Here it is necessary to perform the summation of the luminances of pixels, which are not in the cells themselves, but in special accumulation adders which are situated on the perimeter of the cell medium.

Building of projection for angles 0°, 60°, 120° is quite easy to implement. It is necessary to implement a shift of the entire image in the appropriate directions, typical for this type of

coating. The fig. 3,b shows an example of a direction of shift  $0^\circ$ : each cell ( $x_0$ ) takes the value of its right neighbor ( $x_4$ ). Similarly projections for directions  $60^\circ$  and  $120^\circ$  are constructed.

Projections for angles of  $30^\circ$ ,  $90^\circ$ ,  $150^\circ$  are more complex to build and implement. The difficulty is that it is impossible to perform a shift along the marked directions. To get the desired angles, it is necessary to combine the shift in the neighboring directions in turns by  $0^\circ$ ,  $60^\circ$ ,  $120^\circ$ . Let us consider the example of shift for the angle  $30^\circ$ . When moving left and down, each cell ( $x_0$ ) takes by turns the value of its upper right neighbor ( $x_2$ ) and right neighbor ( $x_4$ ) (fig. 3,c).

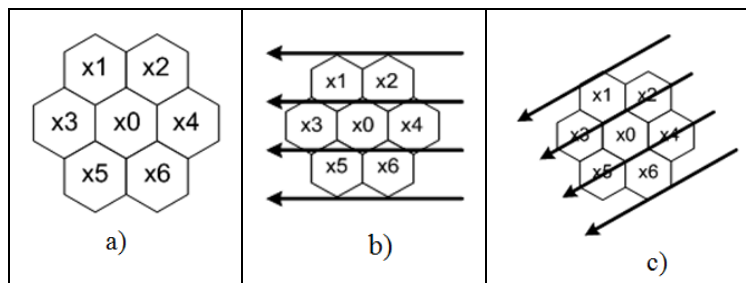


Figure 3: Codes of neighboring cells and shift of the image on the hexagonal cover

Considering all the above, we can describe the principle of operation of the device. Let  $Q$  - set of directions CAHS:  $Q = \{0^\circ, 30^\circ, 60^\circ, 90^\circ, 120^\circ, 150^\circ\}$ . If every line of the  $i$ -th ( $i = \{1, 2, \dots, k\}$ , where  $k$  - the maximum length of the line) in the direction of  $q$  imagine how many pixels  $L_{qi}$ , and such that  $L_{qi} = \{x_1, \dots, x_k\}$ , then You can write the formula amount of luminance values of all pixels in the line

$$S_{qi} = \sum_{j=1}^{Z_i} x_j$$

where  $Z_i$  - the maximum number of pixels in the  $i$ -th line. Then projection RT for direction  $q$  can be represented as an ordered set  $R_q$ , consisting of all sums  $S_{qi}$  this direction:  $R_q = \{S_{q1}, S_{q2}, \dots, S_{qk}\}$ .

Accordingly, a single processing element (PE) of CAHS  $x_0$  at the current time  $t$  ( $x_0(t)$ ) should be set to one of the neighboring PE ( $x_1, x_2, x_3, x_4$ ) in the preceding time  $t-1$  ( $x_{1(t-1)}, x_{2(t-1)}, x_{3(t-1)}, x_{4(t-1)}$ ) under the influence of appropriate control signals ( $SX_1, SX_2, SX_3, SX_4$ ):  $x_{0(t)} = SX_1 \cdot x_{1(t-1)} + SX_2 \cdot x_{2(t-1)} + SX_3 \cdot x_{3(t-1)} + SX_4 \cdot x_{4(t-1)}$ .

In work [15], a comparison of the program models and VHDL-models is performed, and also the analysis of the received projections is carried out. The experiment confirmed the similarity of the projections built during software modeling and Active-HDL models. It is results confirm the possibility of a hardware implementation of RT.

Calculations show that for processing of image with size of  $8192 \times 8192$  pixels (67 megapixels) the cell medium will already spend 0,074 seconds at a frequency 1 MHz. That is,

the performance is sufficient for selection of the characteristic features (CF) on the basis of the RT to build recognition systems that can operate in real time.

Examples of RT for image of letters «A» and 木 for different fonts and noise levels (Fig. 4a) show that this method of selection characteristic features that is resistant to insignificant distortions and noise.

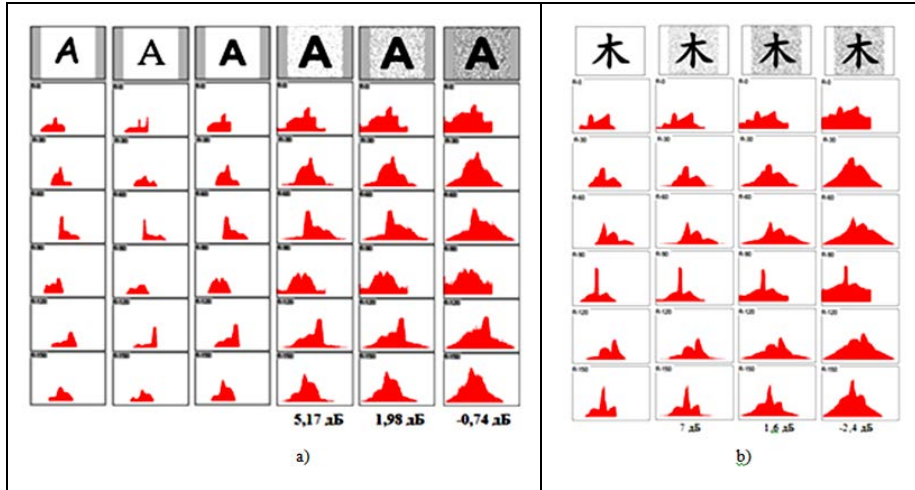


Figure 4: RT for different images letters "A" and the hieroglyph 木

Confident recognition of characters is possible in signal / noise ratio up to level 2dB. We should also mention the peculiarity of RT for finding of straight lines and segments in the image (fig. 4, b). And lines, coinciding with the direction of the slope of the RT, are clearly detected even at signal / noise ratio to -5dB (fig. 4, b).

### 3 Impact of the image rotation on the result of identification based on characteristic feature as RT projections

Since  $\varphi$  – is the angle between the direction of building RT of projection and direction of the coordinate system where there is an image, it does not matter which of these systems is fixed and which rotates. As  $\varphi = 30^\circ$  is not rotated but for normally oriented image ( $0^\circ$ ) of the construction of the RT in the direction of  $30^\circ$ , as well as  $\varphi = 30^\circ$  for reverse other situation - for the image at the angle of  $30^\circ$  in the construction of RT in the direction  $0^\circ$  (In both these cases, the RT formula will look.

$$f_{30}^v(p,30) = R_{30}f = \int_{-\infty}^{\infty} f\left(\frac{\sqrt{3}}{2}p - \frac{1}{2}s, \frac{1}{2}p + \frac{\sqrt{3}}{2}s\right)ds.$$

On the basis of mentioned above CAHS it can be illustrated by constructing of RT projections of the letter «A», which is rotated on  $0^\circ, 5^\circ, 10^\circ, 15^\circ, 20^\circ, 25^\circ$  and  $30^\circ$  (fig. 5), and where for each image a graphical interpretation of the corresponding transformations is shown.

As can be seen from Fig. 5 - RT projection that is rotated on the 30° letter "A" in the direction 0° repeats completely the RT projection of not rotated letter "A" (0°) in the direction 30°.

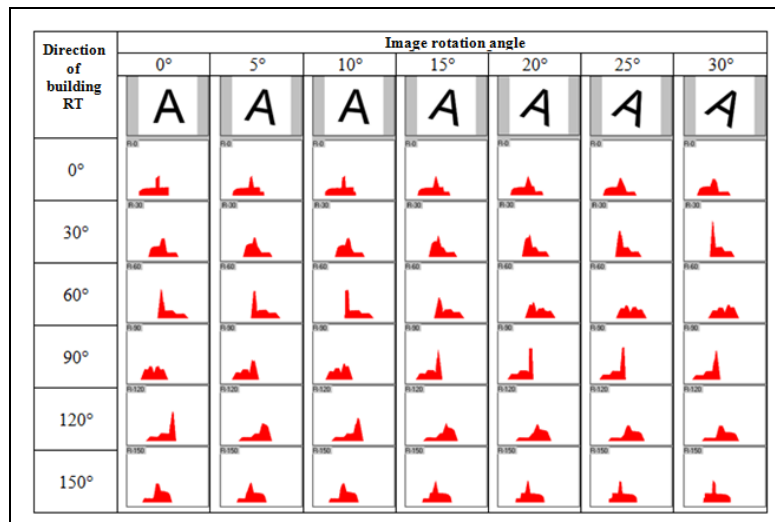


Figure 5: Example implementation of RT for characters with different angles of rotation

Obviously, this regularity is true for any other angles, multiple constructing to RT projections of step. Since the synthesized CAHS selects six projections on RT ranging from 0° to  $\pi$  (RT projection of range from  $\pi$  to  $2\pi$  will be mirror images of the projections in the directions, which are an extension of directions of range from 0° to  $\pi$ ), then step (discrete) of projections constructing is  $\pi/6=30^\circ$ . Thus, selected characteristic features are not sensitive to the rotation of the input angle of image multiple to 30°.

Research has shown that, when it is necessary, to select a larger number RT projections by hardware we can use two or more similar CAHS, which are rotated relative to each other by the angle  $\beta$  (3) along an axis perpendicular to their plane.

For the case of two CAHS on formula (3)  $\angle\beta = 15^\circ$ , we get 12 directions in increments 15° (fig. 6). Fig. 6 indicates by the solid arrows the direction of the first cell medium (CM), is dashes - direction of second CM, which is rotated by an angle relative to the first 15°.

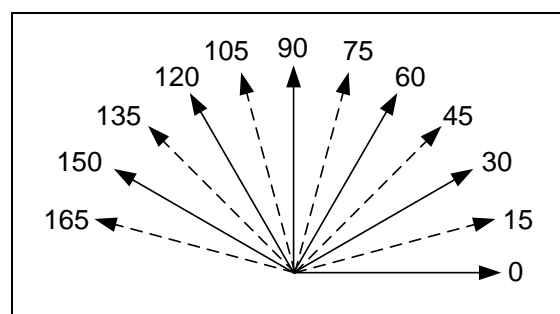


Figure 6: Directions of two CAHS rotated relative to each other on 15°

Thus, multilayer CAHS, which directions are shown in fig. 6 is insensitive to the rotation of the input image on the angle, which multiple to  $15^\circ$ .

The conducted studies has shown, that rotation of the input image at an angle from  $2^\circ$  to  $4^\circ$  has almost no influence on the result of the numbers identification based on characteristic feature as RT projections. The fig. 7 shows examples of RT projections of digit "5", which is normally oriented (fig. 7a) is rotated by an angle of  $2^\circ$  (fig. 7, b) and rotated by an angle of  $4^\circ$  (fig. 7, c). As can be seen from Fig. 7, almost all projections of the direction with the same name are the same.

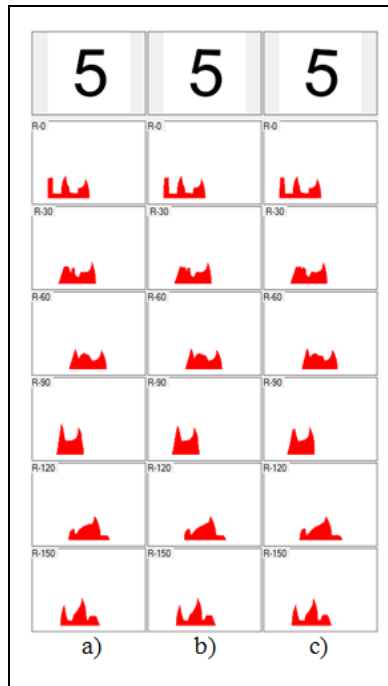


Figure 7: RT projections for the image of digit "5" (a) of rotating on  $2^\circ$  and  $4^\circ$  (b, c)

Taking into account the fact that at rotation of input image a gradual transition of one of selected projection from one discrete value to another (for example in Fig. 5 - by lines), it is possible to use not all full set of CAHS, but the half of the amount with the addition of missed projections with calculated values based on the approximation of neighboring units. In our case for the implementation of constructing of RT projections with increments of  $3^\circ$  (as a middle value between  $2^\circ$  and  $4^\circ$ ) according to (3) it is necessary to use 10 of CAHS. But for the application of the approximating functions it is enough to use CAHS with just 5 layers: hardware will be allocate with the projections by directions  $0^\circ$ ,  $6^\circ$ ,  $12^\circ$ , etc. By approximation we obtain intermediate values  $3^\circ$ ,  $9^\circ$ ,  $15^\circ$ , etc. Thus, such use of the approximation allows to increase the number of allocated projections, while reducing the hardware costs.

The approach based on the use of multilayer CAHS and approximations of the original data allows you to build devices for hardware allocation based on characteristic features of the Radon transform, which is insensitive (invariant) to the rotation of the input image.

## 4 RT Properties under Scaling and Shifting Of the Input Image

It is known, that the Radon transform has the shift and scaling properties [1-3]. The offset function in the spatial domain leads to a displacement of projection along the  $p$ , and its magnitude depends on the angle  $\varphi$  (fig. 2). This is illustrated in fig. 8, where examples of RT for image of the letter "A" are shifted in the directions  $0^\circ$ ,  $45^\circ$  and  $90^\circ$  are shown: value and shape of the projections of the same name are the same, except their displacement. If the direction shift of the input image and built RT projection coincided, the resulting projection did not move at all (fig. 8 a) and b) the projection of R-0 for directions  $0^\circ$ , and a), d) the projection of R-90 for directions  $90^\circ$  ) and most shifted projection that has the perpendicular direction (fig. 8a) and d) of the projection R-0, and a), b) the projection of R-90), which fully confirms the dependence of the displacement of the angle  $\varphi$ .

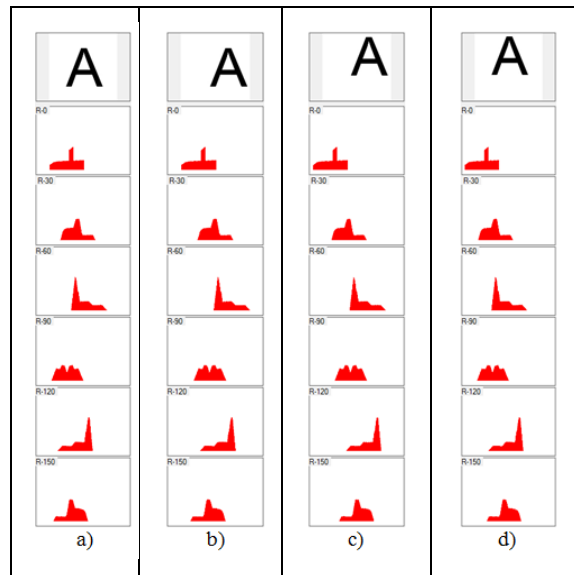
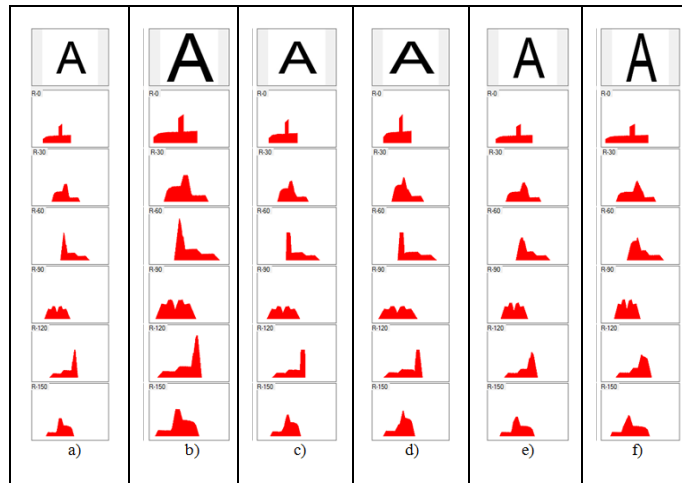


Figure 8: RT projection for image of letters «A» (a) at the shift of direction of the input image  $0^\circ$  (b),  $45^\circ$  (c) and  $90^\circ$  (d)

Similarly to the scaling function in the spatial domain scaling of projections is undergone, but its value does not depend on the angle  $\varphi$ , and completely repeats scaling factor  $m$  of the function itself.

In fig. 9 we show examples of projections of RT for input image of letters «A» (a), which is scaled by proportional with coefficient to  $m = 1,5$  by the two coordinates (b), scaled only in the x-axis (direction CAHS  $0^\circ$ ) with coefficients  $m=1,25$  and  $m=1,5$  (c, d), and the y-axis only (direction CAHS  $90^\circ$ ) with coefficients  $m=1,25$  and  $m=1,5$  (e, f).



**Figure 8: RT projection for image of letters «A» (a) at the shift of direction of the input image 0° (b), 45° (c) and 90° (d)**

As can be seen from Figure. 9 a) and b) – scaling obtained projections of RT repeats completely the proportional scaling of the input image. Thus the sizes of form of the built projections also vary proportionally to  $m$ .

More difficult are the special cases of non-proportional scaling along one of the coordinates (fig. 9, c), d), e), f)), where not only disproportionate strain derived projections are observed, as well as some changes of their shape. For non-proportional scaling of function in the spatial domain of constructed projection is again dependable as in the case of the displacement from angle  $\varphi$ . So, if the direction of non-proportional scaling of the input image and build of RT projection coincide, then the obtained sinogram (fig. 9, a) and c), d) of projection R-0; a) и e), f) of projection R-90) will have the same «width» at extended to  $m$  times in the absolute values. While sinogram of perpendicular direction (fig. 9, a) and c), d) of projection R-90; a) and e), f) of projection R-0) will have an opposite pattern in form of a larger in  $m$  time width and equal to absolute values. Projections for the rest of the intermediate directions will be deformed in both the width and the absolute values on the amount from 1 to  $m$  and will depend on the angle  $\varphi$ . This will be accompanied by some changes in the form, which is explained by the disproportionate change of thickness and inclination angles of elements of the input image at a disproportionate scaled, which generally can be regarded as a kind of deformation or distortion.

Characteristic features in the form of RT projections are invariant to shifts and scaling of the input image. And they also possess resistance to deformation and distortion in the form of non-proportional scaling in one of direction on condition of account of the specification of these cases during operation of comparing of the CF with standard.

## 5 Conclusion

The developed method allows to perform by hardware the selection of characteristic features based on Radon transform, which are insensitive to changes in the input image such as rotation, shift, zoom (including disproportional that is performed in one direction). Moreover, the invariance rotation is ensured by increasing of the number of layers and CAHS approximation of the original data, and the shift and scaling - only through considering when compared with standard characteristics of value of the shift and scaling factor of the input image.

## REFERENCES

- [1]. Radon J. K. A., *Über die Bestimmung von Funktionen durch ihre Integralwerte langs gewisser Mannigfaltigkeiten*, Berichte Sachsische Akademie der Wissenschaften, Leipzig, Mathematisch-Physikalische Klasse, 1917. **69**: p. 262–277.
- [2]. Toft P., *The Radon Transform: Theory and Implementation*. PhD thesis, Dept. of Math. Modelling Section for Digital Signal Processing, Technical Univ. of Denmark, 1996. p. 326.
- [3]. Левин Г.Г., Вишняков Г.Н., *“Оптическая томография”*, Радио и связь, 1989. p. 224.
- [4]. Грузман И.С., *“Математические задачи компьютерной томографии”*. Соросовский образовательный журнал, 2001. **7**(5).
- [5]. Отдыхов Р.Х., Вершок Д.А., *Алгоритм выделения информативных признаков на основе преобразования Радона в системе распознавания рукописных признаков*. Известия НАН Беларуси. Сер. физ.-техн. Наук, 1998. (3): p. 103-107.
- [6]. Варанов В.Г., Храмов А.Г., *Дискретное вверное преобразование Радона в задаче выделения центров ветвей сетчатых структур*. Институт систем обработки изображений РАН “Компьютерная оптика”, 2002. (23): p. 44-47.
- [7]. Кобасяр М.І., Русин В. П., *Детектування кривих з бінарних зображень за допомогою перетворення Радона*. Вісник Національного університету “Львівська політехніка” “Радіоелектроніка та телекомунікації”, 2001. (428): p. 6-9.
- [8]. Вологов Д. В., Гусев В. В., Юрин Д. В., *Обнаружение прямых линий на изображениях на основе преобразования Хартли. Быстрое преобразование Хафа*. 16-я международная конференция по компьютерной графике и ее приложениям, (ГрафиКон2006), Россия, Новосибирск, Академгородок, 2006. с. 182–191.
- [9]. Kadyrov A., Petrou M., *The Trace Transform and Its Applications*. IEEE Ransactions On Pattern Analysis And Machine Intelligence, 2001. **23**(8): p. 811-828.
- [10]. Von Neumann J., *Theory of Self-Reproducing Automata: Edited and completed by A. Burks.*, University of Illinois Press, 1966.

- [11]. Zuse K., *Calculating Space*. Translated from German. – Tech. Transl. AZT-70-64- GEMIT. – MIT Project MAC, 1970.
- [12]. Ulam S., *Random Processes and Transformations*. Proceedings Int. Congr. Mathem, 1952. (2): p. 264-275.
- [13]. Blanchard F., et al., *Topological and Measure-Theoretic Properties of One-Dimensional Cellular Automata*. Physica D: Nonlinear Phenomena, 1997. **103**(1-4): p. 86-99.
- [14]. Belan S., *Specialized cellular structures for image contour analysis*, Cybernetics and Systems Analysis, 2011. **47**(5): p. 695-704.
- [15]. Belan S., and Motornyuk R., *Extraction of characteristic features of images with the help of the radon transform and its hardware implementation in terms of cellular automata*. Cybernetics and Systems Analysis, 2013. **49**(1): p. 7-14.
- [16]. Wolfram S., *Cellular Automata*. Los Alamos Science, 1983. **9**: p. 2-21.
- [17]. Nicoladie D. Tam., *Hexagonal pixel-array for efficient spatial computation for motion-detection pre-processing of visual scenes*, Advances in image and video processing, 2014. **2**(2): p. 26-36.
- [18]. Wolfram S., *Random Sequence Generation by Cellular Automata*. Advances in Applied Mathematics, 1986. **7**: p. 429 – 432.

# Performance Improvement by Sorting the Transform Coefficients of Host and Watermark using Unitary Orthogonal Transforms Haar, Walsh and DCT

H. B. Kekre<sup>1</sup>, Tanuja Sarode<sup>2</sup>, Shachi Natu<sup>3</sup>

<sup>1</sup>Senior Professor, MPSTME, NMIMS University Mumbai, <sup>2</sup>Associate Professor, TSEC, Mumbai University, Mumbai, <sup>3</sup>Ph. D. Research Scholar, NMIMS University, Mumbai;  
hbkekre@yahoo.com, tanuja\_0123@yahoo.com, shachi\_natu@yahoo.com

## ABSTRACT

This paper proposes a new watermarking technique in which host and watermark image is converted to frequency domain using orthogonal transforms Haar/Walsh/DCT. These transforms are applied fully, row wise and column wise to host and watermark. Transform coefficients of host image are sorted in descending order of energy and replaced by sorted transform coefficients of watermark. Column and row transforms of Haar, Walsh and DCT prove better over full transform. Further, sorting results in better imperceptibility as it minimizes the energy difference between original host's transform coefficients and replaced watermark coefficients. Proposed technique gives better performance than unsorted transform coefficients for watermarking. In this paper results of only Haar transform are given due to space limitation.

**Keywords:** Watermarking, column transform, row transform, cropping, binary distributed run length noise, Gaussian distributed run length noise, resizing.

## 1 Introduction

Reproduction of digital contents has become easier due to various tools available for it. At the same time demand for transmission of digital contents is growing rapidly. This makes it compulsory to have protection of data in terms of prevention from illegal copying or distribution. Watermarking serves the purpose for the same.

Watermarking refers to insertion of signature of owner of digital contents into those contents itself. It should satisfy two major constraints. First is invisibility (imperceptibility) which means original digital contents and contents after insertion of watermark should look same to the Human Visual System. Second is robustness against various attacks which try to

destroy or remove the watermark [1]. Insertion of watermark can be done in two different domains namely spatial and frequency domain.

- Spatial domain watermarking:

Watermarking in spatial domain refers to modification to the pixel values of specific region of an image [2]. Apart from the advantage of simplicity, the major drawback of spatial domain watermarking techniques is its poor capability to embed data and less robustness to attacks. LSB technique is widely appreciated spatial domain technique. Various other spatial domain techniques have been proposed in [1, 2, 3, 4].

- Frequency domain watermarking:

Watermarking in frequency domain refers to transforming host image into frequency domain and modifying transform coefficients by watermark [3]. By applying inverse transform watermarked image is obtained. Image can be transformed into frequency domain using transforms like Discrete Cosine Transform (DCT), Discrete Fourier Transform (DFT), and Discrete Wavelet Transform (DWT) etc. Multiple watermarks can also be embedded in different frequency locations of host image to provide more robustness.

A DCT based watermarking technique is given by W. Lu et. al in [5] where watermark is embedded into the DCT coefficients of sub images which are obtained by subsampling the original image. In [4], Riaz et. al proposed a frequency domain watermarking in which encrypted data is inserted into the image. Extraction is usually the reverse procedure of insertion. Circular watermarking by amplitude modulation is proposed by Licks in [6]. The best known technique of watermarking is proposed by Cox [7] by applying DCT to the entire image. Wavelet based watermarking is proposed by Woo et. al in [8] and by Giakoumaki in [9]. Kekre, Sarode and Shachi natu have proposed DCT wavelet, Walsh wavelet and hybrid wavelet based watermarking techniques in [10-18].

In this paper, a frequency domain blind watermarking technique for digital images is proposed. It uses Haar, Walsh and Discrete Cosine transform. These transforms are applied to host images as well as to watermark to be embedded. Along with the full transform, row transform and column transforms are also used using Haar, Walsh and DCT. Transformed watermark elements are sorted and are inserted in sorted middle frequency elements of transformed host image. Varying embedding energy of watermark is used to test the robustness against various attacks by keeping in mind energy conservation property of transforms. Organization of paper is as follows. Section 2 describes proposed method. Section 3 describes results and observations for the proposed method and compares proposed work with our previous work in which watermark is inserted in frequency domain without sorting the frequency coefficients. Section 4 concludes the paper.

## 2 Proposed method

In proposed method orthogonal transforms DCT, Walsh and Haar are explored in full, column and row version along with the concept of sorting elements of middle frequency band of host and frequency elements of watermark.

Transformed image obtained after applying full transform to it is given by

$$F=T*f*T^t \quad (1)$$

Where, T is unitary, orthogonal transform matrix, T' is its transpose, f is image to be transformed and F is transformed image. Original image can be obtained from transformed image as

$$f=T^t * F * T \quad (2)$$

For column transform, transformed image is obtained by premultiplying image with transform matrix as shown in equation (3) and original image is obtained by premultiplying transformed image with transpose of transform matrix as shown in equation (4).

$$F=T*f \quad (3)$$

$$f=T^t * F \quad (4)$$

Row transform of an image is given by operating transposed transform matrix on rows of an image and image in spatial domain is obtained by operating transform matrix on rows of transformed image as shown in equation (5) and (6).

$$F=f*T^t \quad (5)$$

$$f=F*T \quad (6)$$

We have explored various orthogonal transforms for embedding watermark without sorting transform coefficients. It was found that Haar column transform is strongly robust against various attacks like cropping, noise addition, compression, resizing etc. also it was closely followed by Haar row transform and then by column and row versions of Walsh and DCT. Hence in this paper emphasis is on checking the performance of these transforms against various attacks when host and watermark frequency coefficients are sorted based on energy. Figure 1

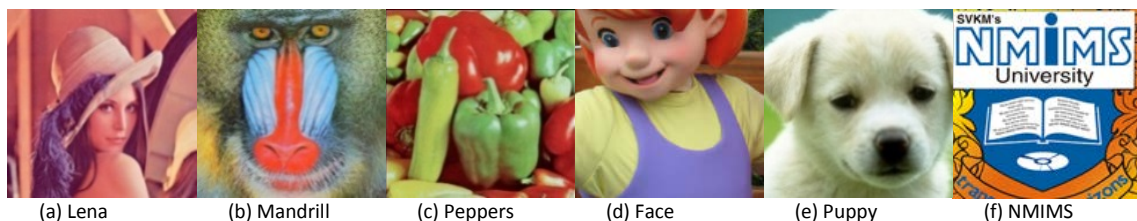


Figure1: Host images and a watermark image used for experimental work

## 2.1 Embedding Process:

1. Read host image and watermark image.
2. Take Haar/Walsh/Discrete Cosine Transform (full/ column/ row) of them.
3. For full transform select HL and LH band to embed the watermark. For column transform middle rows and for row transform middle columns are selected for embedding watermark.
4. Elements of watermark as well as elements from the frequency band of host are sorted in descending energy order.
5. Sorted frequency elements are normalized and scaled using suitable scaling factor such that watermark energy is 60%, 100% and 140% of the mid-frequency band energy of host.
6. Mid-frequency coefficients of host are replaced by scaled and sorted frequency elements of watermark.
7. Inverse transform is taken to obtain watermarked image.

## 2.2 Extraction process:

1. Read watermarked image.
2. Apply Haar/ Walsh/ DCT (full/ column/ row) to it.
3. Sort middle frequency elements of transformed watermarked image.
4. From these middle frequency elements recover frequency elements of watermark. these elements are descaled, denormalized and placed in their respective places after inverse sorting.
5. Reconstruct watermark from recovered elements by taking inverse transform.

Sorting of host and watermark frequency elements leads to minimization of energy difference between original and replaced elements and thus reduces the error between host and watermarked image.

## 3 Results of proposed method against various attacks

Results of proposed method are shown in terms of recovered watermark from attacked image and they are compared to results of watermarking without energy sorting of frequency elements of host and watermark images. Due to limitation of space results of only Haar transform for Lena image are shown.

Figure 2(a) and (b) show watermarked image Lena using full transform HL band and recovered watermark from it obtained using proposed method with sorting and unsorted coefficients.

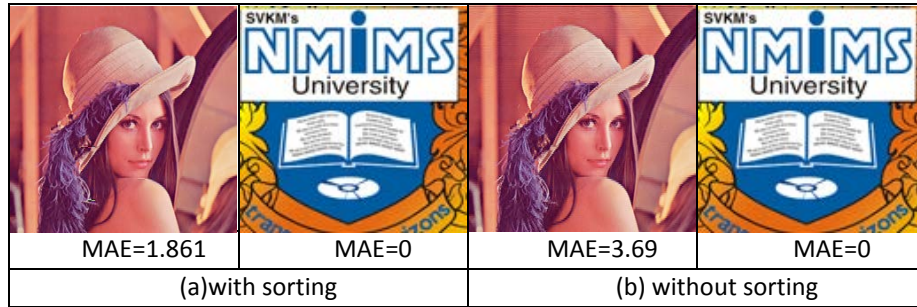


Figure 2: Watermarked Lena image and recovered watermark from it with and without sorting using HL band to embed the watermark

From Figure 2 we can see that MAE between host image and watermarked image has been reduced resulting in better imperceptibility. Figure 3 shows the similar results when LH band is used to embed the watermark. Here also, using sorted transform coefficients results in better imperceptibility.

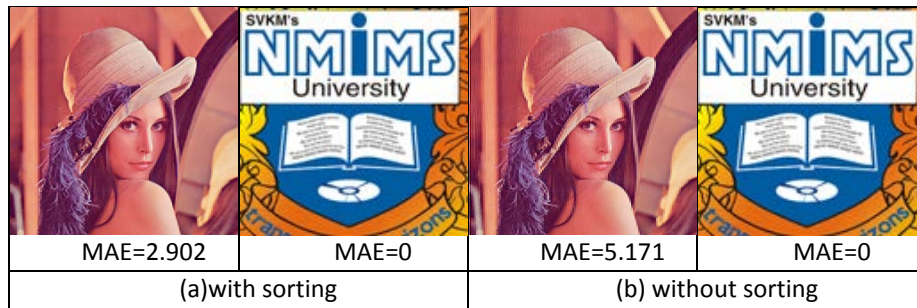


Figure 3: Watermarked Lena image and recovered watermark from it with and without sorting using LH band to embed the watermark

Figure 4 (a) shows watermarked image and recovered watermark from it using column Haar transform when sorting is performed on transform coefficients and Figure 4(b) shows the result obtained without sorting. Figure 5(a) shows watermarked image and recovered watermark from it when row Haar transform is used and transform coefficients are sorted. Figure 5(b) shows corresponding images for unsorted transform coefficients.

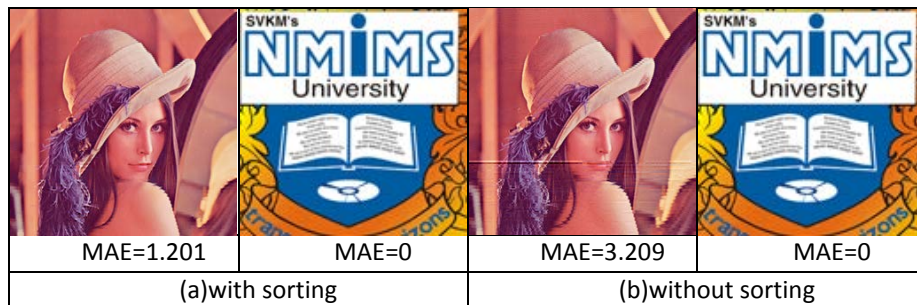


Figure 4: Watermarked image and recovered watermark from it using column Haar transform

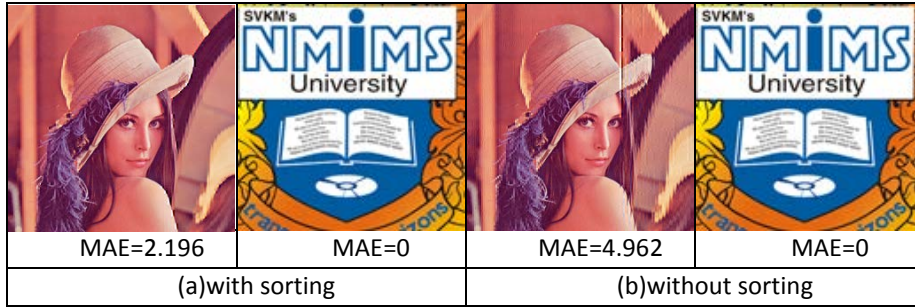


Figure 5: Watermarked image and recovered watermark from it using row Haar transform

From Figure 4 and Figure 5 it is very clear that sorting improves the imperceptibility of watermarked image.

### 3.1 Performance evaluation of proposed method against various attacks:

From Figure 2- Figure 5, it can be concluded that using sorted coefficients, better imperceptibility can be achieved. Another important thing observed in Figure 2- Figure 5 is that column transform gives the highest imperceptibility among all. In the following sections we focus on robustness of proposed method by evaluating its performance against various attacks. Various attacks performed on watermarked images are cropping, compression, noise addition, histogram equalization and resizing. These attacks except histogram equalization are performed in variety of ways. For e.g. compression attack is performed using various transforms like DCT, DST, Walsh, Haar, JPEG compression and Vector quantization based compression.

#### 3.1.1 Results of cropping attack:

Figure 6 shows results of cropping a watermarked image at four corners (16x16) using full Haar transform and column and row version of Haar transform.

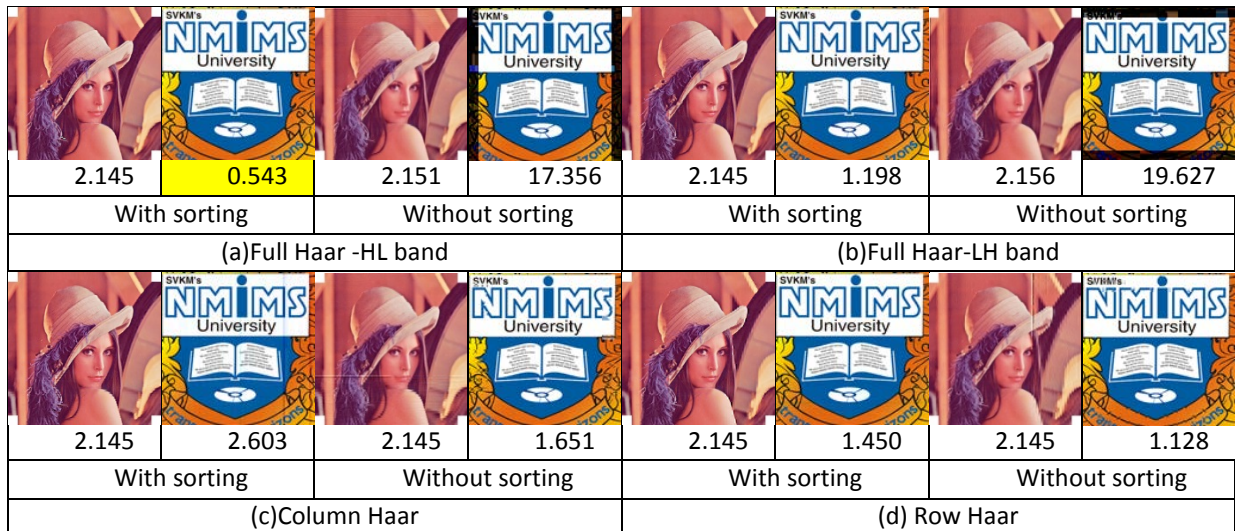


Figure 6: Watermarked image and recovered watermark from it when 16x16 cropping is performed with and without sorting transform coefficients: (a) Full transform HL band (b) Full transform LH band (c) Column transform (d) Row transform

Figure 6 shows that in sorting method, HL band when used for embedding the watermark gives minimum MAE between embedded and recovered watermark. This error is much less than the error when transform coefficients are not sorted. For LH band used for watermark embedding also similar effect is observed. However, the trend of reduction in error does not follow for column and row transform.

### 3.1.2 Compression attack:

Compression attack using various orthogonal transforms, using vector quantization and JPEG compression is performed on watermarked images. Results of DCT based compression, JPEG compression and VQ based compression with and without sorting technique are shown in Figure 7 to Figure 9 respectively.

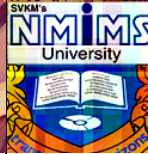
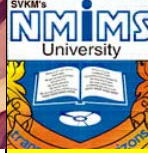
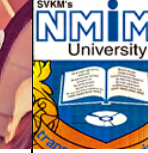
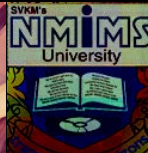
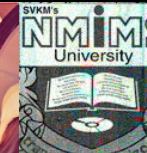
							
1.179	30.939	1.515	47.539	1.574	24.108	1.708	39.536
With sorting		Without sorting		With sorting		Without sorting	
(a) Full Haar -HL band				(b) Full Haar-LH band			
							
0.717	8.812	0.897	24.685	1.076	11.938	1.391	31.028
With sorting		Without sorting		With sorting		Without sorting	
(c) Column Haar				(d) Row Haar			

Figure 7: Watermarked image and recovered watermark from it when compression using DCT is performed with and without sorting transform coefficients: (a) Full transform HL band (b) Full transform LH band (c) Column transform (d) Row transform

From Figure 7, it is observed that sorting the transform coefficients for embedding reduces the MAE between embedded and recovered watermark. Among them, Column version of transform is more robust followed by row transform than other versions (full HL and Full LH).

Figure 8 shows watermarked images after JPEG compression and recovered watermark from it. Column Haar transform proves to be more robust for JPEG compression attack and column as well as row transform with sorted coefficients give better imperceptibility and robustness than in case of unsorted elements. However, full transform with sorted transform coefficients does not give better robustness than full transform with unsorted coefficients.

							
1.958	108.470	2.086	45.474	2.386	64.501	2.225	50.078

With sorting		Without sorting		With sorting		Without sorting	
(a)Full Haar -HL band				(b)Full Haar-LH band			
1.962	17.623	1.974	30.450	1.981	22.698	2.125	33.578
With sorting		Without sorting		With sorting		Without sorting	
(c)Column Haar.				(d) Row Haar			

Figure 8: Watermarked image and recovered watermark from it when JPEG compression is performed with and without sorting transform coefficients: (a) Full transform HL band (b) Full transform LH band (c) Column transform (d) Row transform

Figure 9 shows watermarked images compressed using Vector Quantization performed using KFCG algorithm [19] with codebook size 256. Full transform with sorted coefficients give less distorted image than in case of unsorted coefficients but due to color changes it shows high MAE between embedded and recovered watermark. Recovered watermark quality is better in column and row Haar transform using sorted coefficients and row transform shows minimum MAE value i.e. strong robustness among all.

2.494	103.939	2.525	43.262	2.650	48.669	2.590	35.625
With sorting		Without sorting		With sorting		Without sorting	
(a)Full Haar -HL band				(b)Full Haar-LH band			
2.468	24.018	2.522	37.361	2.546	23.577	2.608	28.905
With sorting		Without sorting		With sorting		Without sorting	
(c)Column Haar 2.				(d) Row Haar			

Figure 9: Watermarked image and recovered watermark from it when VQ compression is performed with and without sorting transform coefficients: (a) Full transform HL band (b) Full transform LH band (c) Column transform (d) Row transform

### 3.1.3 Noise addition attack:

Addition of noise to image during its transmission is yet another common attack possible after compression. In the proposed method binary distributed run length noise and Gaussian distributed run length noise are introduced and are added to watermarked image. Binary distributed noise has magnitude 0 and 1 with normal distribution. Different run lengths of binary distributed noise are tried like run length 1 to 10, 5 to 50 and 10 to 100. Gaussian distributed run length noise has discrete magnitude between -2 and 2. Figure 10 shows noise added watermarked images with binary run length noise (run length 10 to 100) and recovered watermarks. From Figure 10 it can be seen that sorting gives better robustness in all cases.

Among them full transform with LH band gives zero error followed by row transform, full transform HL band and column transform.

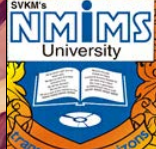
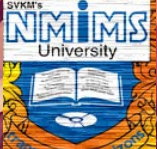
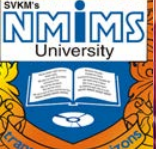
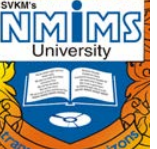
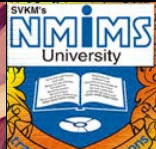
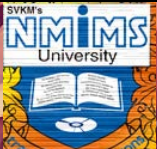
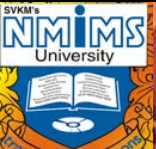
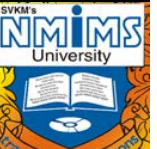
							
1	4.838	1	20.234	1	0	1	0
With sorting		Without sorting		With sorting		Without sorting	
(a) Full Haar -HL band				(b) Full Haar-LH band			
							
1	7.356	1	13.284	1	0.192	1	0.472
With sorting		Without sorting		With sorting		Without sorting	
(c) Column Haar				(d) Row Haar			

Figure 10: Watermarked image and recovered watermark from it when binary distributed run length noise is added with and without sorting transform coefficients: (a) Full transform HL band (b) Full transform LH band (c) Column transform (d) Row transform

Figure 11 shows watermarked images when Gaussian distributed run length noise is added to it and recovered watermark from it. It is observed that sorting coefficients in HL band gives best robustness among all. It is also equal to the performance of embedding in unsorted coefficients. For LH band of full transform as well as row and column transform, robustness improves when transform coefficients are sorted.

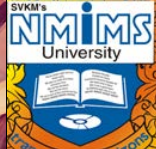
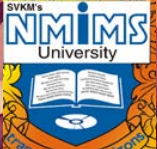
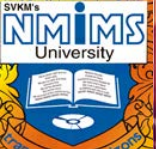
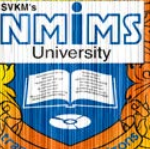
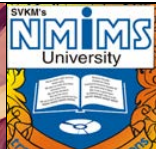
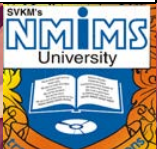
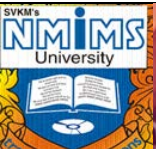
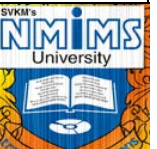
							
0.746	0	0.746	0	0.746	3.047	0.746	15.144
With sorting		Without sorting		With sorting		Without sorting	
(a) Full Haar -HL band				(b) Full Haar-LH band			
							
0.746	0.142	0.746	0.358	0.746	4.683	0.746	9.088
With sorting		Without sorting		With sorting		Without sorting	
(c) Column Haar				(d) Row Haar			

Figure 11: Watermarked image and recovered watermark from it when Gaussian distributed run length noise is added with and without sorting transform coefficients: (a) Full transform HL band (b) Full transform LH band (c) Column transform (d) Row transform

### 3.1.4 Image resizing attack:

In resizing attack watermarked image is zoomed to double its size and then resized to its original size using techniques like bicubic interpolation, grid based interpolation [20] and orthogonal transform based zooming [21]. Figure 12 shows result images for zoomed-reduced watermarked images using bicubic interpolation and recovered watermarks from them for full, column and row Haar transform. As can be seen from Figure 12, in each case (full, column and row) sorting of transform coefficients results in better robustness. Row Haar transform shows better robustness among all when sorting is used.

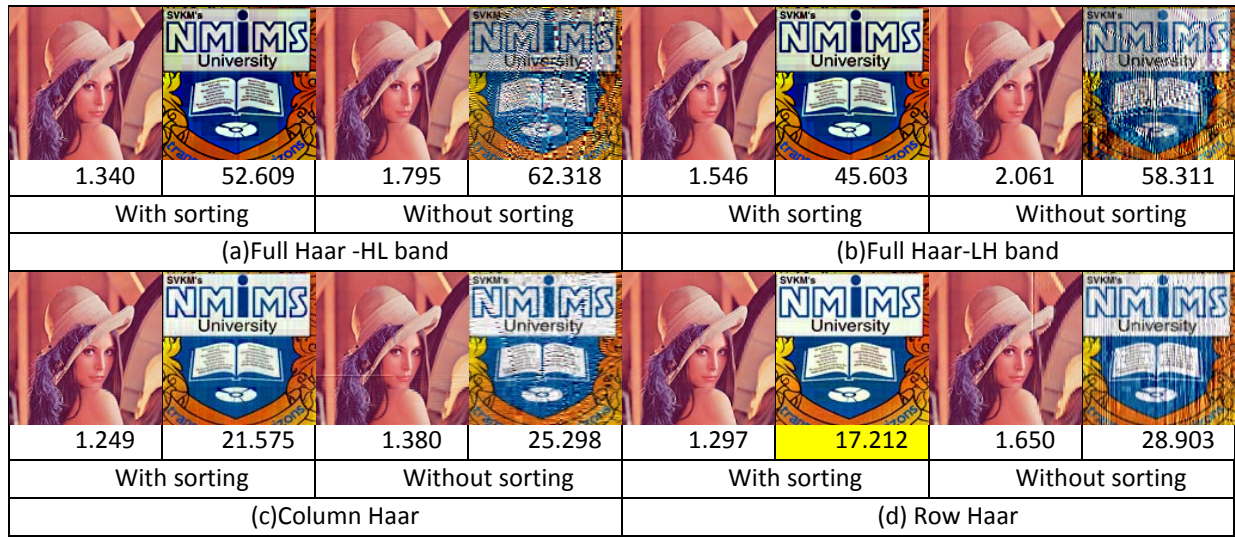
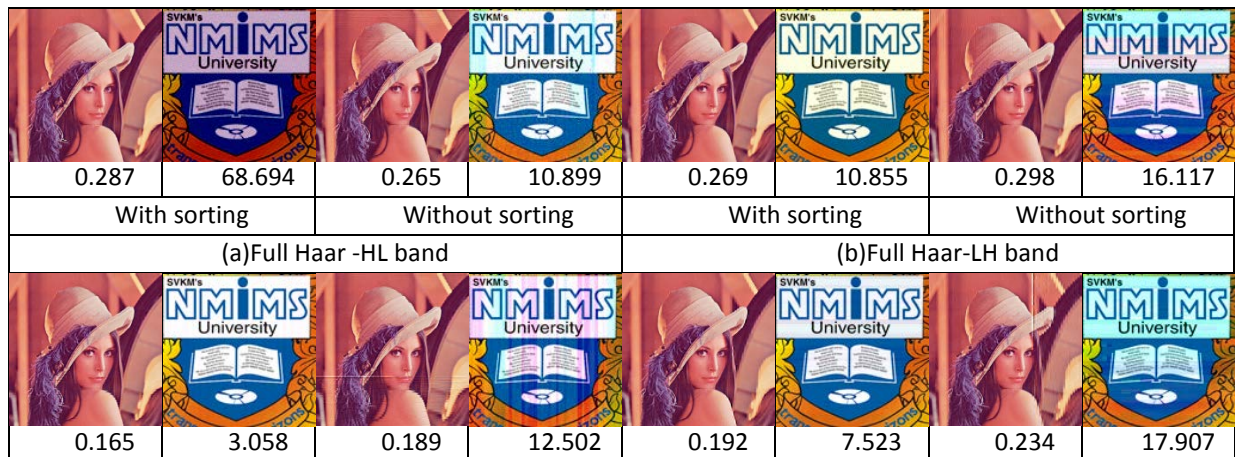


Figure 12: Zoomed-reduced Watermarked image and recovered watermark from it using bicubic interpolation with and without sorting transform coefficients: (a) Full transform HL band (b) Full transform LH band (c) Column transform (d) Row transform

Figure 13 shows resizing attack performed using grid based interpolation technique and recovered watermarks from it. Column Haar transform with sorted transform coefficients gives more robustness than full and row transform. Full transform using LH band for embedding the watermark also shows reduced MAE between embedded and recovered watermark. But full transform using HL band for embedding watermark fails to give robustness as it shows strong color manipulation taking place in recovered watermark.



With sorting	Without sorting	With sorting	Without sorting
(c) Column Haar		(d) Row Haar	

Figure 13: Zoomed-reduced Watermarked image and recovered watermark from it using grid based interpolation with and without sorting transform coefficients: (a) Full transform HL band (b) Full transform LH band (c) Column transform (d) Row transform

Figure 14 shows resized watermarked images using Discrete Fourier transform and recovered image from them. For full transform HL and LH band sorting of transform coefficients improves robustness as well as imperceptibility. For column transform robustness almost remains same in both the cases and for row transform again it shows minor improvement in robustness.

0.149	1.462	0.337	9.587	0.252	1.535	0.335	6.725
With sorting		Without sorting		With sorting		Without sorting	
(a) Full Haar -HL band				(b) Full Haar-LH band			
0.156	1.345	0.135	1.337	0.137	0.909	0.128	1.369
With sorting		Without sorting		With sorting		Without sorting	
(c) Column Haar				(d) Row Haar			

Figure 14: Zoomed-reduced Watermarked image and recovered watermark from it using DFT based zooming with and without sorting transform coefficients: (a) Full transform HL band (b) Full transform LH band (c) Column transform (d) Row transform

### 3.2 Performance comparison of proposed technique with technique using unsorted transform coefficients for various attacks.

In Figure 15, graph of comparison of full Haar transform HL band with and without sorting and 100% embedding energy is shown for various attacks performed on watermarked Lena image. Performance of proposed sorting technique is better for every attack performed on watermarked image prominently except for resizing using grid based interpolation, VQ based compression and JPEG compression and to very small extent for 32x32 cropping at center.

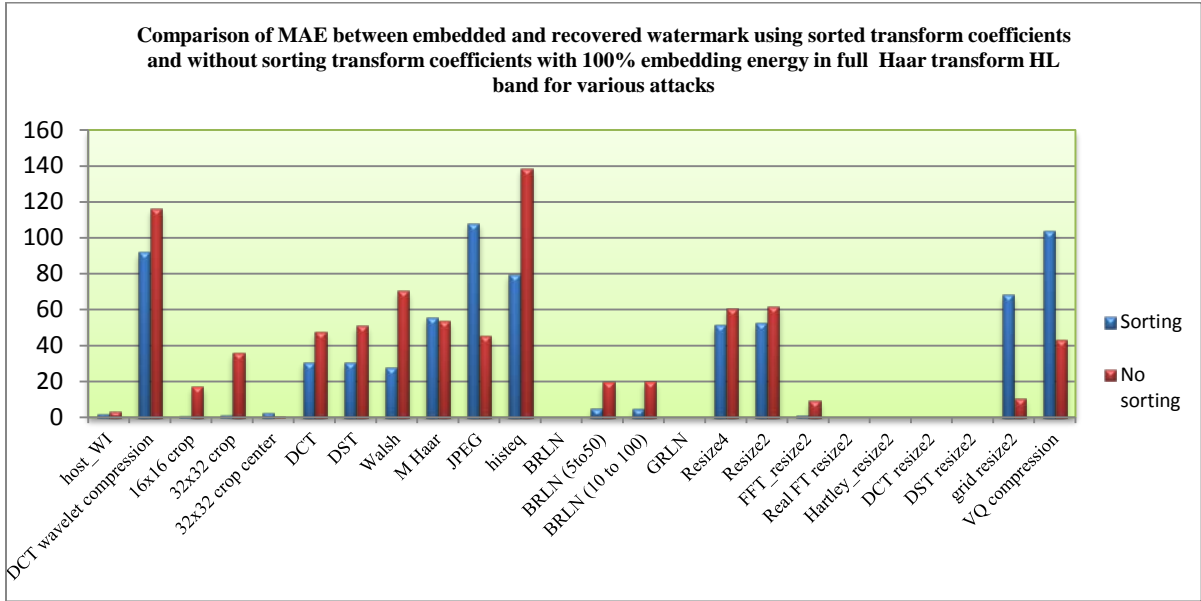


Figure 15: Performance comparison of full Haar transform HL band with embedding energy 100% with and without using sorting for 'Lena' image

Figure 16 shows graph of MAE comparison when full Haar transform is taken and LH band is selected to embed the watermark after sorting transform coefficients. For LH band also sorting results in better robustness. An improvement seen in LH band embedding is that for grid based resizing method sorting technique gives better robustness than without sorting the transform coefficients. For VQ based compression and JPEG compression, sorting does not prove effective than unsorted coefficients.

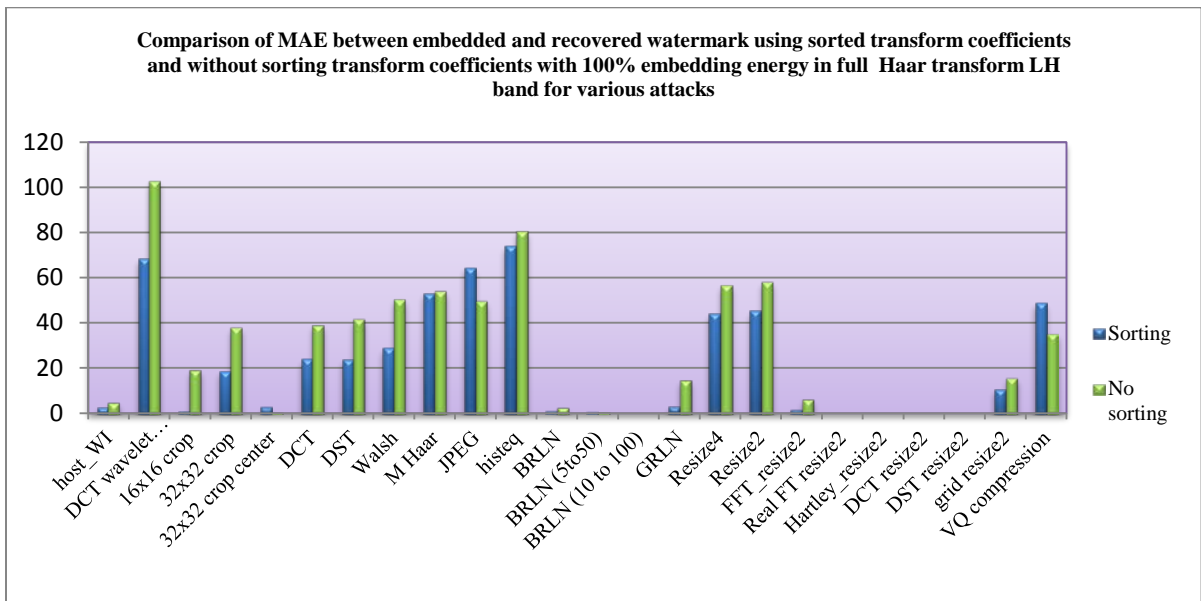


Figure 16: Performance comparison of full Haar transform LH band with embedding energy 100% with and without using sorting for 'Lena' image

Graphs in Figure 17 and Figure 18 show comparison of MAE between embedded and recovered watermark for various attacks when column and row Haar transforms are used

respectively both with and without sorting of transform coefficients and 100% embedding energy. Both column and row transform show significant improvement in robustness with sorting over HL and LH band of full transform for JPEG compression, VQ based compression and grid based resizing attack. For other attacks also it gives better robustness than unsorted transform coefficients.

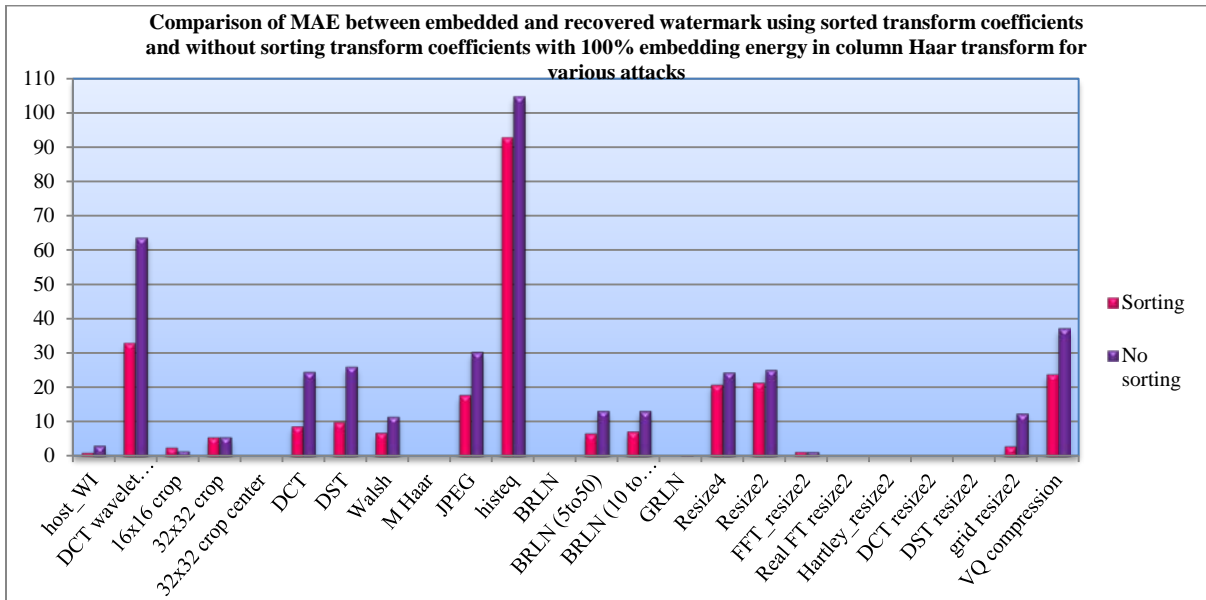


Figure 17: Performance comparison of column Haar transform with embedding energy 100% with and without using sorting for 'Lena' image

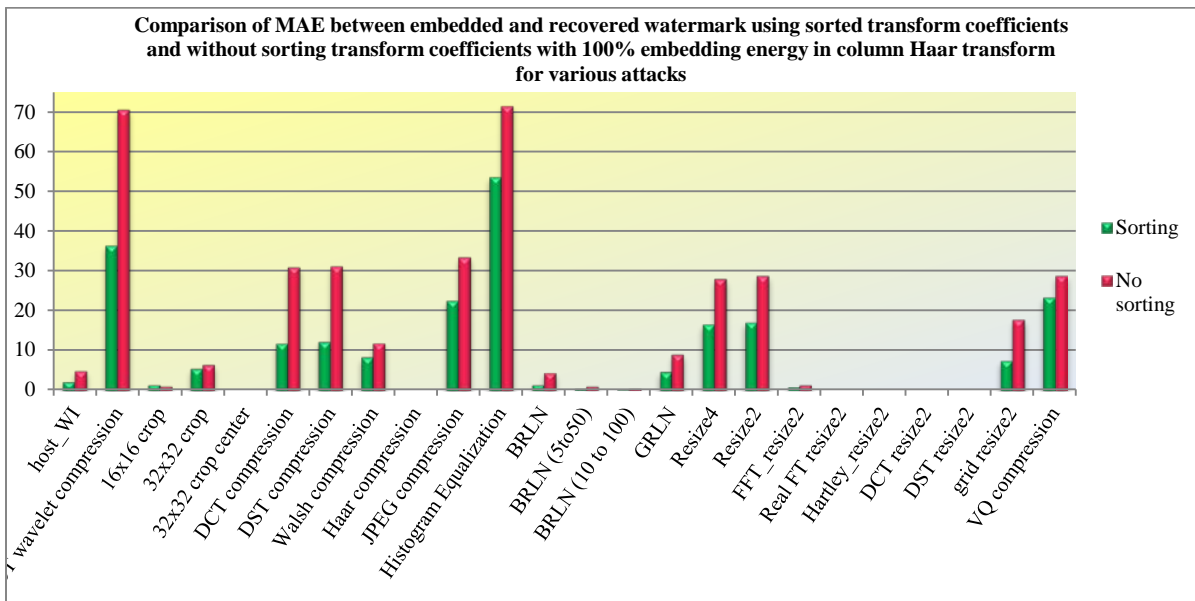


Figure 18: Performance comparison of row Haar transform with embedding energy 100% with and without using sorting for 'Lena' image

## 4 Conclusion

Sorting of transform coefficients of watermark and host minimizes the error between corresponding elements and hence overall error of embedding the watermark. Full Haar HL band results in better robustness than in case where transform coefficients are not sorted except JPEG and VQ compression attack and grid based resizing. Full Haar LH does better by eliminating grid base resizing from the above list. Column and row Haar transform are proved better in terms of robustness than full transform (HL and LH band). This is true for other transforms explored i.e. Walsh and DCT too.

## REFERENCES

- [1]. Houtan Hadded Larijani, Gholamali Rezai Rad, "A new spatial domain algorithm for gray scale images watermarking", In proc. of international conference on computer and communication engineering, pp. 157-161, May 2008.
- [2]. Rajesh Kannan Megalingam, Mithun Muralidharan Nair, Rahul Srikumar, Venkat Krishnan Balasubramanian, Vineeth Sarma Venugopala Sarma, Chapter titled, "Novel Variance based Spatial Domain Watermarking and its Comparison with DIMA and DCT based Watermarking Counterparts", in the book, "Applications of MATLAB in Science and Engineering", ISBN 978-953-307-708-6, Intech Open Access Publisher, 2011, ch. 22, pp. 451-468
- [3]. Ibrahim Nasir, Ying Weng, Jianmin Jiang, "A new robust watermarking scheme for color image in spatial domain", In proc. of third international conference on signal image technologies and internet based systems, pp. 942-946, 2008.
- [4]. Saba Riaz, Yonus Javed, M. Almas Anjum, "Invisible watermarking schemes in spatial and frequency domains", In proc. of 4th international conference on emerging technologies, pp. 211-216, 2008.
- [5]. W. Lu, H Lu and F. L. Chung, "Robust digital image watermarking based on subsampling", Applied mathematics and computation, vol. 181, pp.886-893, 2006
- [6]. V. I. Licks, "On digital image watermarking robust to geometric transformations", Master of science Electrical engineering, university of New Mexico, 2000.
- [7]. I. Cox, J. Killian, T. Leighton and T. Shamoan, "Secure spread spectrum watermarking for multimedia", IEEE transaction on image processing, 6(12), 1673-1687, December 1997.
- [8]. C. S. Woo, J. Du, B. Pham, "Performance factor analysis of a wavelet based watermarking methods", in Proc. of Australian information security workshop, vol. 44, pp. 89-97, Feb. 2005.
- [9]. A. Giakoumaki, S. Pavlopoulo, D. Koutouris, "A medical image watermarking scheme based on wavelet transforms", In proc. of 25<sup>th</sup> annual international conference of the engineering in medicine and biology society, IEEE, vol. 1, pp.856-859, September 2003.
- [10]. H. B. Kekre, Tanuja Sarode, Shachi Natu, "Performance Comparison of DCT and Walsh Transforms for Watermarking using DWT-SVD", International Journal of Advanced Computer Science and Applications, Vol. 4, No. 2, pp. 131-141, 2013.

- [11]. Dr. H. B. Kekre, Dr. Tanuja Sarode, Shachi Natu, "Hybrid Watermarking of Colour Images using DCT-Wavelet, DCT and SVD", *International Journal of Advances in Engineering and Technology*, vol.6, Issue 2. May 2013.
- [12]. Dr. H. B. Kekre, Dr. Tanuja Sarode, Shachi Natu, "Robust watermarking using Walsh wavelets and SVD", *International Journal of Advances in Science and Technology*, Vol. 6, No. 4, May 2013.
- [13]. Dr. H. B. Kekre, Dr. Tanuja Sarode, Shachi Natu, "Performance Comparison of Wavelets Generated from Four Different Orthogonal Transforms for Watermarking With Various Attacks", *International Journal of Computer and Technology*, Vol. 9, No. 3, pp. 1139-1152, July 2013.
- [14]. Dr. H. B. Kekre, Dr. Tanuja Sarode, Shachi Natu, "Performance of watermarking system using wavelet column transform under various attacks", *International Journal of Computer Science and Information Security*, Vol. 12, No. 2, pp. 30-35, Feb 2014.
- [15]. Dr. H. B. Kekre, Dr. Tanuja Sarode, Shachi Natu, "Robust watermarking scheme using column DCT wavelet transform under various attacks", *International Journal on Computer Science and Engineering*, Vol. 6, No. 1, pp. 31-41, Jan 2014.
- [16]. Dr. H. B. Kekre, Dr. Tanuja Sarode, Shachi Natu, "Performance evaluation of watermarking technique using full, column and row DCT wavelet transform", *International Journal of Advanced Research in Electrical, Electronics and Instrumentation Engineering*, Vol. 3, Issue 1, Jan 2014.
- [17]. Dr. H. B. Kekre, Dr. Tanuja Sarode, Shachi Natu, "Robust watermarking technique using hybrid wavelet transform generated from Kekre transform and DCT", *International Journal of Scientific Research Publication*, vol. 4, Issue 2, pp. 1-13, Feb 2014.
- [18]. Dr. H. B. Kekre, Dr. Tanuja Sarode, Shachi Natu, "Effect of weight factor on the performance of hybrid column wavelet transform used for watermarking under various attacks", *International Journal of Computer and Technology*, Vol. 12, No. 10, pp. 3997-4013, March 2014.
- [19]. H. B. Kekre, Archana A. Athawale, Dipali Sadavarti, "Algorithm to Generate Kekre's Wavelet Transform from Kekre's Transform", *International Journal of Engineering, Science and Technology*, (IJEST) Vol. 2(5), 756-767, 2010.
- [20]. H. B. Kekre, Tanuja Sarode, Sudeep Thepade, "Grid based image scaling technique", *International Journal of Computer Science and Applications*, Volume 1, No. 2, pp. 95-98, August 2008.
- [21]. Dr. H. B. Kekre, Dr. Tanuja Sarode, Shachi Natu, "Image Zooming using Sinusoidal Transforms like Hartley, DFT, DCT, DST and Real Fourier Transform", selected for publication in *International journal of computer science and information security* Vol. 12 No. 7, July 2014.

# Study of Erosion Processes in the Tinto Salt-Marshes with Remote Sensing Images

**Emilio Ramírez-Juidías**

*School of Agricultural Engineering, Universidad de Sevilla, SPAIN;*  
[erjuidias@us.es](mailto:erjuidias@us.es)

## ABSTRACT

Both climatic factors and the sea wave energy are two important factors to study the tidal wetlands. One of the most important wetlands in the Southwest of the Iberian Peninsula is the Tinto salt-marshes, the third largest wetland in Andalusia after Doñana and Odiel salt-marshes. From 1956 to 2010 the land use changes (LUC) have given rise to a great landscape transformation that along with the effects of recent climate change, have caused a strong impact on the environment. With the development of image processing techniques and use of unmanned aerial vehicles (UAVs) is possible to obtain patterns of erosion sufficiently precisely. In this paper, a new methodology patented by the author is presented and used to obtain the total volume of eroded soil in the Tinto salt-marshes. In the same way, the different causes that give rise to this phenomenon as well as the influence of intertidal processes are discussed. The results shown how the erosion processes are an immediate consequence of the low kinetic energy in the Tinto river and hence of the progressive increase of the negative rate of eroded soil.

**Keywords:** Unmanned aerial vehicle, Eroded soil, Wave energy, Wetlands.

## 1 Introduction

According to [1], concern over sediment and erosion has shifted recently from on-site effects on productivity and engineering stability to downstream influences on in-stream and estuarine ecosystems. Human activity has caused hitherto the acceleration of both sediment and erosion processes as well as other also negative, so that wetlands have lost much of its original area [2, 3].

Although ecosystem processes with their implications for the future progress of land degradation have been studied at numerous field sites around the world, it is difficult to extrapolate findings from field studies at patch scale in other areas [4, 5]. Though satellite platforms may contribute to the solution of this problem, the use of UAVs presents an

important advantage because it allows us to represent all the topographical features of the salt-marshes, which are often insufficiently reflected in conventional contour lines mapping [6, 7], thereby supplying the spatial information needed for marshes-scale analyses of the relationships between climate change and soil erosion.

In Tinto salt-marshes, the residence times of sediment in their river system are long with much intermediate storage of eroded material, as is common to most large river systems around the world, and as occurs in Australia [1]. By the other hand, increased storage of sediment can result in substantial changes to Tinto river's physical form and their ecological health. This last aspect is very important as a consequence of the importance of this river to the study of life in extreme conditions. In addition, there is no doubt that within Tinto river system there is a great diversity of impacts of the changed sediment regime.

A further consequence of long residence times in rivers, and according to [1], is that the major historical changes will continue to influence river behavior for many decades to come. Likewise, this makes it crucial for us to predict the trajectory of response to historical change, being the temporal scale of analysis of decades or longer due to the great relevance of the net response of sediment to the distribution of floods over many years.

Hitherto, most remote sensing studies have attempted to approach loss soil and their erosion processes solely through mapping changes in vegetation cover and abundance, or LUC in general sense, and even with different methods capable of derive state variables based on the reflectance characteristics of soils [4] and/or the characteristics of the vegetable canopy. However, although the use of UAVs can be considered recent, the percentage of published papers is much greater perhaps it can be due to the huge potential of UAVs in the different techniques used in remote sensing.

The quantification of erosion processes through UAVs, with the help of ground work, can provide new required insights to predict the total volume of eroded soil not only in any wetland but also elsewhere of the world. However, when the area is compound for a complex network of catchments and/or aquifers, it is necessary to use high-resolution orthophotography. A feasible solution is the use of new images processing techniques, which are nowadays accepted by the scientific community.

## **2 Materials and Methods**

### **2.1 Study Area**

The Tinto salt-marshes (Figure 1), with a total area of 32,867,946.31 m<sup>2</sup>, are located in the province of Huelva (Southwest of the Iberian Peninsula), associated to Tinto river mouth. These salt-marshes are located to 3.5 km of Odiel salt-marshes.

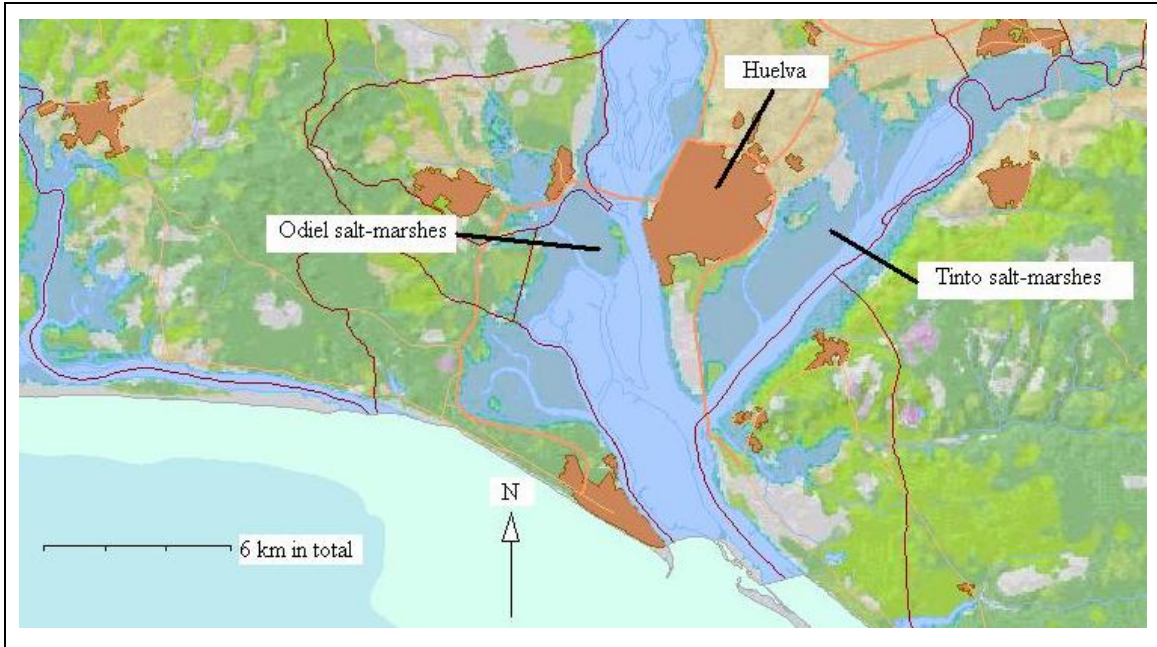
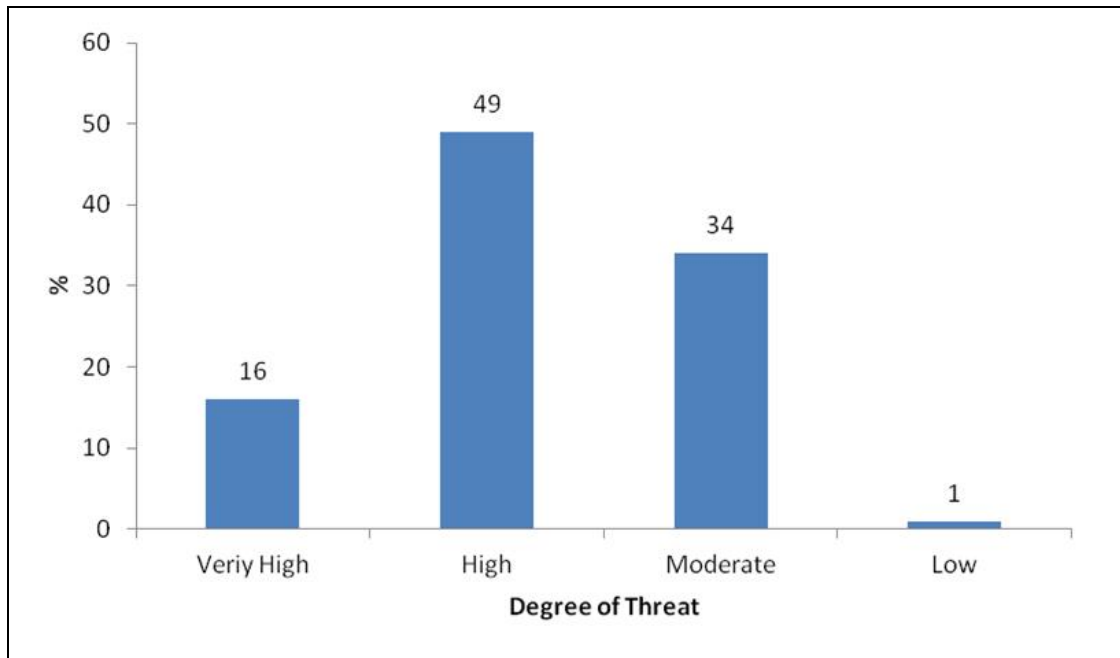


Figure 1: Location of Study Area

According to [7], the area is integrated in a complex system of estuaries of recent sedimentation influenced, in their genesis, by level changes of Earth's crust [8]. All set is surrounded by Tertiary formations of yellow silt and Miocene marls, Pliocene sands and marls, and remains of a Pleistocene erosive glacia. In the Tinto salt-marshes are given simultaneously both sedimentation and erosion processes that vary in space and time, creating a lot of temporary or permanent physiographic characteristics giving rise to a considerable variety of habitats. The tidal movement is the main determining factor in shaping of these ecosystems.

The area consists of a tidal marsh area well preserved and another area, Dehesa de Alquería, where both forest and dry-land crops are predominant. The part of dry land located to the North consist of clayey soils on which run a small stream whose mouth give rise to the formation of two small freshwater lagoons where every year an abundance of ducks, geese, and swans overwinter, and is used as breeding area by wading birds, small-to medium-sized ground-living birds (*Rallidae* or rails), ducks, geese, and swans.

In the environment there is high anthropic influence. Tinto salt-marshes are close to the Tartessos' Industrial Park, where raw sewage and solid waste pour into the area from the National Cellulose Company. In the West is located the solid waste landfill of Huelva, where abunds discharges of rubble due to the existence of the brownfield site. The vulnerability of the area depending on the risk of threat to natural habitats is shown in Figure 2.



**Figure 2: Surface's Distribution by Degree of Threat**

In another vein, the climate in the study area can be defined as mediterranean maritime, with and insolation grade exceeding 3,000 h/year. In the winter season, notable for a short period of low temperatures, most of the rains occur. On the other hand, the summers are dry and long though smoothed out by the proximity of the ocean, not exceeding, usually, the absolute maximum temperature of 44 °C. The average annual rainfall is 483.922 mm, being concentrated in the months of December and January, presenting, likewise, a dry season with deficient water balance between the months from May to September [7].

## 2.2 Data and Methodology

For the investigation was necessary to establish a total of 23 control points distributed within the study area (Figure 3), all of them identified by georeferenced photogrammetric images for the initial period 1973 to 2010 obtained from Iberpix (National Geographic Institute of Spain). Likewise, during the month of September 2013, images were acquired of the study area via an UAV, which were georeferenced in the European Terrestrial Reference System 1989 (ETRS-89). The UAV was equipped with a miniature radar system capable of collect and record the different points of study area.

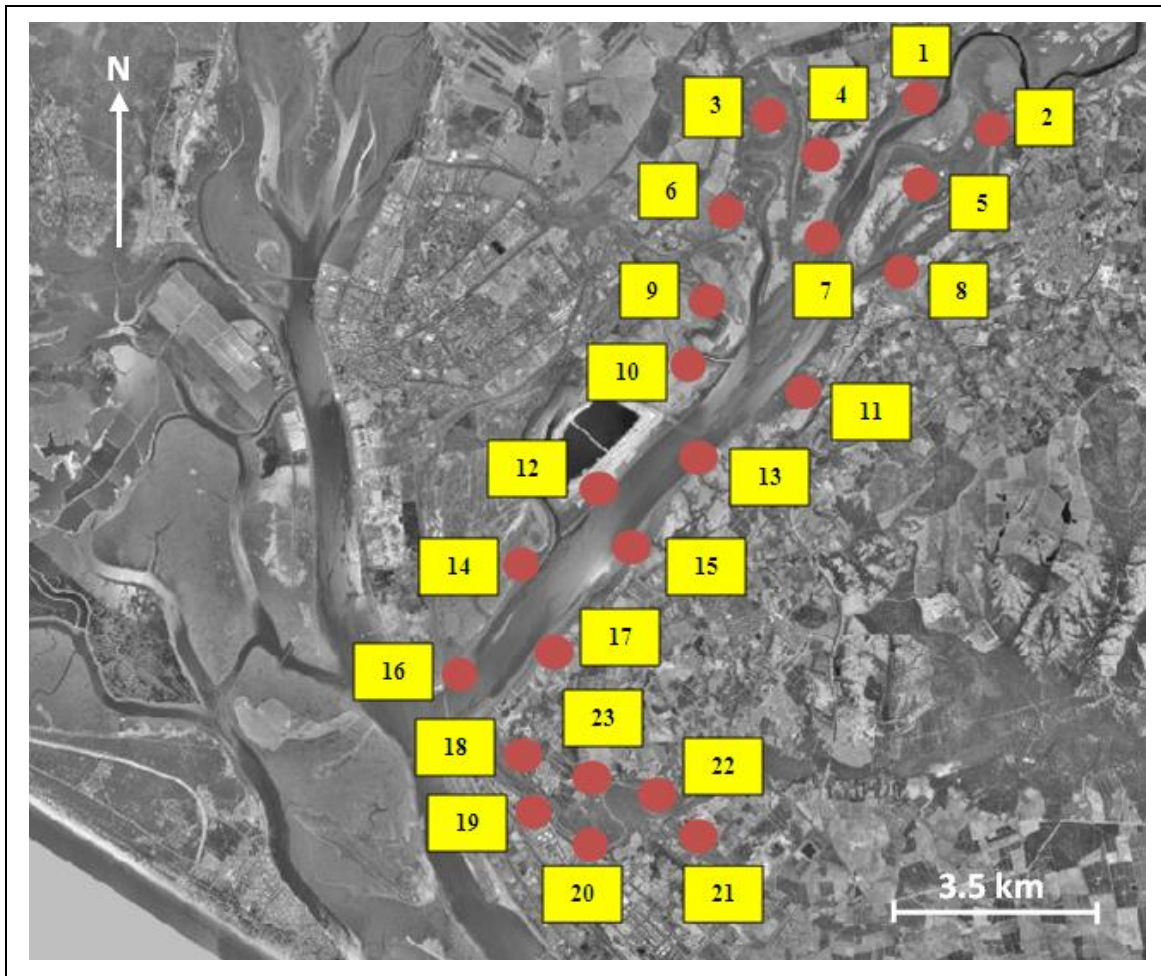


**Figure 3: Distribution of Control Points in the Study Area**

To obtain a good analysis of the study area it was necessary establishing two periods of time into the initial established period (1973-1985 and 1985-2010), which was compared with the data collected in situ via UAV in September 2013 to be able to obtain the total volume of eroded soil in Tinto salt-marshes.

For each period all images, including the UAV images, were orthorectified with a 25 (first period 1973-1985), 10 (second period 1985-2010) and 5 (UAV data) m resolution digital elevation model (DEM) belonging to Andalusian Government (second period) and the National Geographic Institute of Spain (all other periods). These DEM's provide suitable resolution to obtain the different levels of Tinto salt-marshes with the help of the control points selected within the study area [9] and iterative processes [10]. Also through iterative processes were obtained, in each pixel of both photogrammetric and UAV images, the average water depth of Tinto salt-marshes in each period, which was necessary to obtain the eroded soil in these salt-marshes.

According to [7], an additional deep literature review was completed aimed to determine the possible existence of a temporal record of precipitation in the Tinto salt-marshes broad enough to obtain results, discussions and conclusions coherent with the present study. In this

regard the precipitation data was analyzed from meteorological stations located in Lepe, Moguer, Almonte and Doñana salt-marshes in order to predict the precipitation data in Tinto salt-marshes from 1900 to 2010 (Figure 4) starting from the correlation among the different meteorological stations ( $r = 0.92$ ).

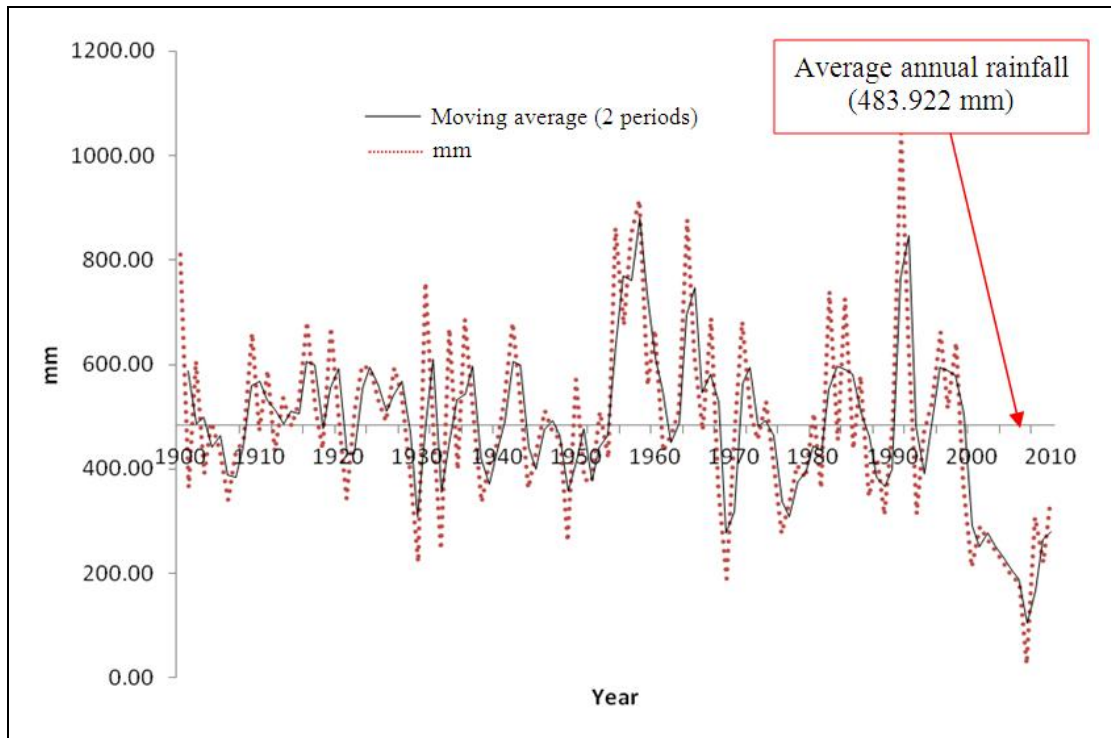


Figure 4: Estimated Rainfalls in the Study Area

### 3 Results and Discussion

#### 3.1 Land Use Changes

Regarding altered or constructed areas, and after conducting a detailed study of web master service (WMS) layers obtained from REDIAM (REd De Información AMBiental de Andalucía “Environmental Information Network of Andalusia”) for the period from 1956 to 2007, can be appreciated (Figure 5) a significant increase of these areas ( $6,544 \cdot 10^4 \text{ m}^2$  in 1960s,  $16,237 \cdot 10^4 \text{ m}^2$  in 1990s and  $22,323 \cdot 10^4 \text{ m}^2$  in 2000s) due to the expansion of the urban fabric and the construction of new housing estates, mainly on the coast [11], where the built-up area has increased six-fold due to tourism development, intensive agriculture and rising industrialized areas.

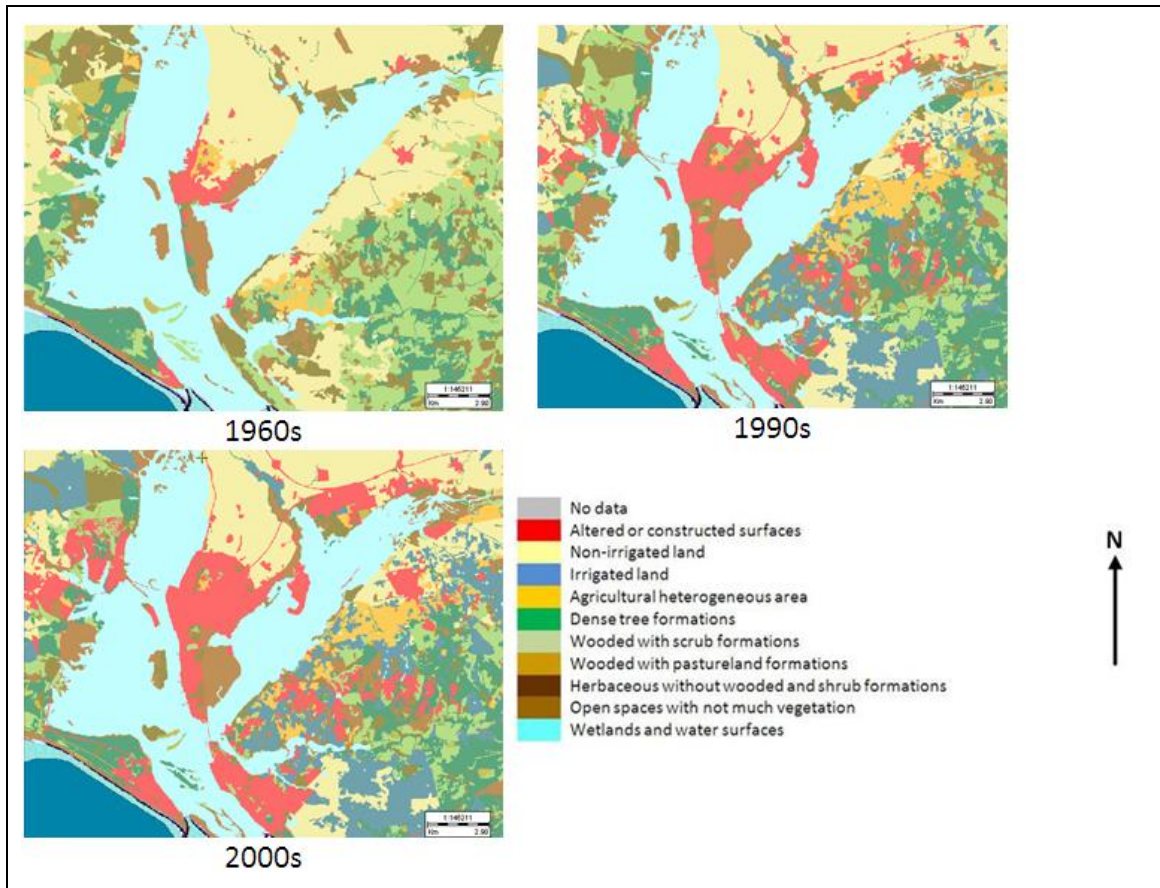


Figure 5: Land Use Changes in the Study area for 1960s, 1990s and 2000s

In respect to agricultural area there was a decline of  $3 \cdot 10^7 \text{ m}^2$  between 1956 and 2007. The evolution followed by different rain fed lands has been uneven, while the arable crops area has remained relatively stable, the extent of other crops has experienced sharp decreases, so that the total area has lost 23 % of its original extent. Noted is the drastic reduction of crops' mosaics and natural vegetation, which record the loss of 60 % of the area occupied in 1956 [11].

In contrast to the abandonment or conversion to forest uses rain fed crops, the area dedicated to irrigation has increased to over  $43 \cdot 10^7 \text{ m}^2$  in 2007, mainly emphasizing greenhouse crops and citrus located in the municipalities of Almonte, Lepe, Lucena del Puerto, Gibraleón, Cartaya, Palos de la Frontera and Moguer [11].

In another vein, wetlands and water surfaces had a slight increase of  $2,564 \cdot 10^4 \text{ m}^2$  between 1956 and 2007, registering the major changes in littoral wetlands, being the total area 9 % lower than its original extent ( $33 \cdot 10^7 \text{ m}^2$  in 1956).

The loss of wetlands and littoral water areas is related to the LUC produced in both Odiel and Tinto salt-marshes. According to [12] the biggest changes in tidal marshes have been for their suitability as industrial salinas and aquatic park crops in Odiel salt-marshes, the arrow of El Rompido and the mouth of the Guadiana river' ( $44 \cdot 10^5 \text{ m}^2$  in 1956 and  $17 \cdot 10^6 \text{ m}^2$  in 2007).

The LUC of forestry and natural areas have particular importance given the size of these spaces in the province of Huelva ( $778,921 \cdot 10^4 \text{ m}^2$  in 1960s,  $784,322 \cdot 10^4 \text{ m}^2$  in 1990s and  $763,533 \cdot 10^4 \text{ m}^2$  in 2000s due to their conversion in agricultural areas). According to [12], the reforestations (mostly eucalyptus) carried out explain the evolution followed by wooded forest area in the study area, as well as the loss of a third of the  $306,126 \cdot 10^4 \text{ m}^2$  occupied in 1956 by treeless scrub formations.

Finally, it is important to mention the two processes that accelerate the conversion of forest stands in scrub areas or pastureland and therefore the change of typology within the LUC of forestry and natural areas, i.e., forest fires (nearly  $7,889 \cdot 10^4 \text{ m}^2$  between 1999 and 2007) and the oak decline of *Quercus* (this disease causes the death of both holms and cork oaks and reduces the economic profitability of the dehesa) [11].

### 3.2 Prediction of the Volumetric Change Processes

After analyzing the meteorological data it was determined [5] that a correlation between precipitation data from Doñana and Tinto were sufficiently significant ( $\leq 0.001$ ) to obtain an equation to predict the data presented in Figure 6.

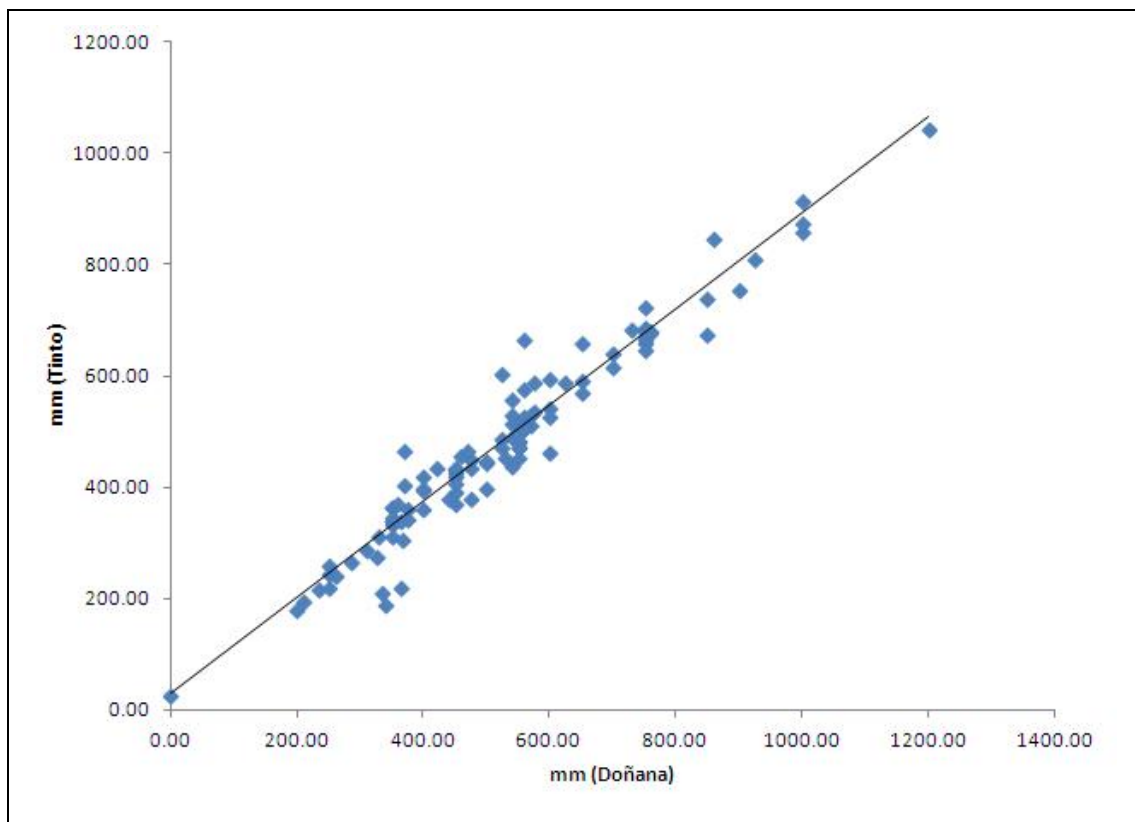


Figure 6: Adjusted Regression Curve for Rainfall Data in Tinto Salt-Marshes

The equation is:

$$y = 354.936 + 0.857 \times P - 0.165 \times A \tag{1}$$

$$r = 0.97$$

$$R^2 = 0.94$$

Where “y” is the prediction of rainfall in the Tinto salt-marshes in mm, “P” is the rainfall data in Doñana salt-marshes in mm and “A” is the year.

According to [7], and after analyzing photogrammetric images, a progressive decrease in annual water surface was obtained in Tinto salt-marshes, to be main causes, on one hand the increase of human activity around of study area, and moreover the cumulative decrease of rainfall, which indicates (Figure 5) that the environment of Tinto is under the influence of a dry period.

The Tinto salt-marshes area analysis showed that the 1960s had the most water surface that the 1990s and 2000s, with no significant differences between 1990s and 2000s.

The 32,867,946.31 m<sup>2</sup> of Tinto salt-marshes, corresponding to the maximum area flooded, are equivalent to a maximum volume of 48.35·10<sup>6</sup> m<sup>3</sup> after performing the prediction.

After extrapolating data from photogrammetric images to Ilwis GIS, was carried out a joint analysis using different DEM to estimate the depth of the study area. Likewise, and for each period and UAV data, according to [5], significant relationships were observed (Table 1) between the volume of water and the Tinto salt-marshes surface, not becoming part of the model the estimated depth perhaps due to the peculiarities of the Tinto river and its importance for the study of life in extreme conditions, resulting in that the anthropic factor may be low enough so as to influence its variation along with tides. Table 1 also shows estimated volume and area equation in Tinto salt-marshes for each period.

**Table 1: Prediction of volume in each period according to the DEM used (“y” is the prediction of volume in the Tinto salt-marshes in hm<sup>3</sup> and “S” is the estimated surface in these salt-marshes in km<sup>2</sup>)**

Period	DEM used	Equation	Significance
<b>1973-1985</b>	25 m	$y = -8.615 + 1.633 \times S$ $r = 0.98$ $R^2 = 0.91$ <span style="float: right;">(2)</span>	≤0.001
<b>1985-2010</b>	10 m	$y = -8.227 + 1.613 \times S$ $r = 0.98$ $R^2 = 0.91$ <span style="float: right;">(3)</span>	≤0.001
<b>UAV data</b>	5 m	$y = -8.627 + 1.635 \times S$ $r = 0.98$ $R^2 = 0.92$ <span style="float: right;">(4)</span>	≤0.001

The estimated depth (Table 2) was obtained through iterative processes using a total of five hundred random sample points selected in the photogrammetric images, a necessity to identify the eroded soil in these salt-marshes.

**Table 2: Summary of estimated depth in each control point and in each DEM used**

Control point nº	Estimated depth (m) in each DEM used			Control point nº	Estimated depth (m) in each DEM used		
	25 m	10 m	5 m		25 m	10 m	5 m
<b>1</b>	0.16	0.16	0.16	<b>13</b>	3.08	3.05	3.07
<b>2</b>	0.32	0.24	0.30	<b>14</b>	3.08	3.08	3.10
<b>3</b>	0.33	0.33	0.38	<b>15</b>	3.10	3.09	3.10
<b>4</b>	1.20	0.77	1.07	<b>16</b>	3.10	3.10	3.11
<b>5</b>	1.50	1.35	1.68	<b>17</b>	3.11	3.11	3.11
<b>6</b>	1.70	1.60	1.73	<b>18</b>	3.19	3.15	3.18
<b>7</b>	2.00	1.85	1.98	<b>19</b>	3.21	3.20	3.23
<b>8</b>	2.45	2.23	2.42	<b>20</b>	3.22	3.22	3.22
<b>9</b>	2.78	2.62	2.81	<b>21</b>	3.23	3.23	3.23
<b>10</b>	2.95	2.87	3.00	<b>22</b>	3.24	3.24	3.24
<b>11</b>	3.00	2.98	3.04	<b>23</b>	3.31	3.28	3.30
<b>12</b>	3.02	3.01	3.03	-	-	-	-

Also, one-way analysis of variance for correlated samples [13] was carried out for the estimate depth in each period, whose result is shown in Table 3.

**Table 3: ANOVA summary for estimated depth**

	SS	df	MS	F	P
<b>Treatment (between groups)</b>	0.0775	2	0.0387	10.47	0.000191
<b>Error</b>	0.1647	44	0.0037	-	-
<b>Blocks (periods)</b>	74.4531	22	-	-	-
<b>Total</b>	74.6953	68	-	-	-

Likewise, and in order to check the differences between periods, a Tukey HSD test was completed, where was observed a significant difference ( $p \leq 0.01$ ) between period 1 (1973-1985) and 2 (1985-2010), and between period 2 and 3 (UAV data), an expectable result as a consequence of the different DEMs used. However, the interaction between period 1 and 3 is non-significant, probably because the UAV was so high (50 m above ground) that it was able to capture the density of marsh vegetation in full, resulting a random resemblance to the model obtained in the first period. This in turn is related to the middle of the second period, with establishment in the area of the figure of natural landscape, giving rise to strong ecological

preservation for the purpose of maintaining the marsh, reason that in 2013 the model is very similar to the first period (in this period the low density of buildings and population in areas close to Tinto salt-marshes gave rise to its almost complete ecological maintenance).

### 3.3 Prediction of the Erosion in Tinto Salt-Marshes

Sediment transport was obtained between consecutive periods through pixel evaluation in Tinto salt-marshes by contrast of the different DEMs used (Figure 7). In this Figure 7 is simulated the sediment transport for the total of study period starting from the characteristics (rainfall and temperature) of each period.

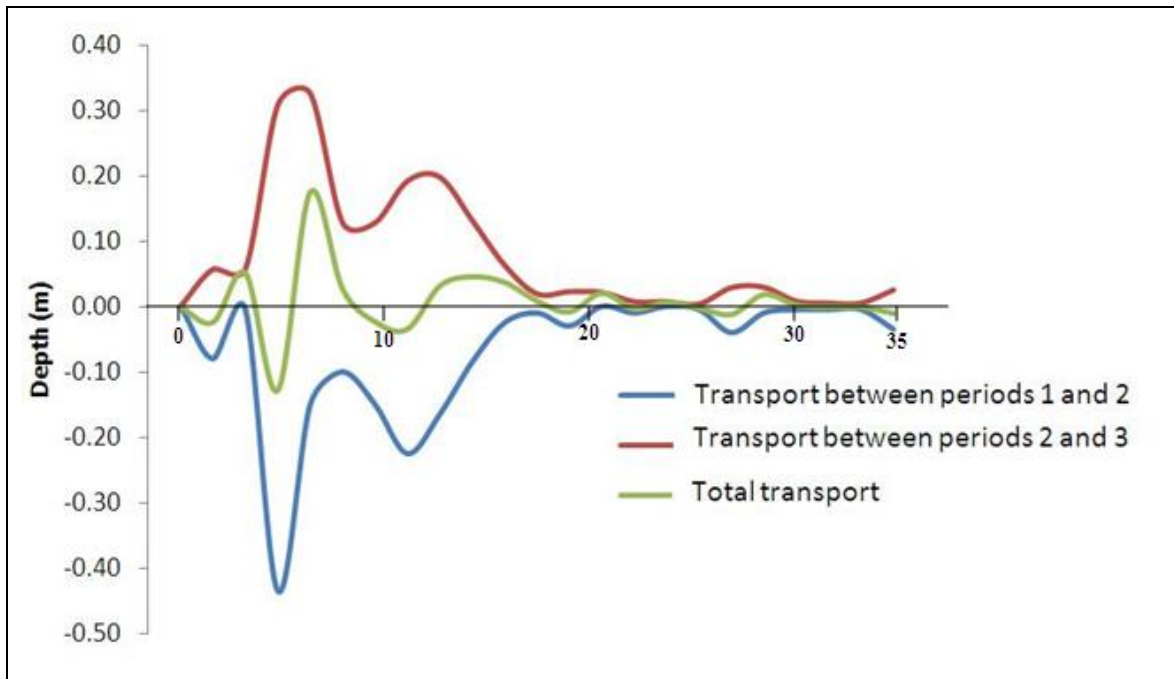


Figure 7: Depth Variations in Tinto Salt-Marshes by Sediment Transport During the Study Period (35 years)

After, a multiple linear regression was applied to all data obtained to be able to predict the total volume of eroded soil (Equation 5) in the study period. Further, the original images were classified using [14] (Figures 8 and 9).

$$y = 0.008 - 0.563 \times SD + 2.903 \times T \quad (5)$$

$$r = 0.937$$

$$R^2 = 0.867$$

Where “y” is the prediction of total volume of eroded soil in the Tinto salt-marshes in  $\text{hm}^3$ , “SD” is the equivalent area, in  $\text{km}^2$ , in which has occurred the volume of eroded soil, and which has caused an increase or decrease in the level “T” of the bed of Tinto salt-marshes in m.

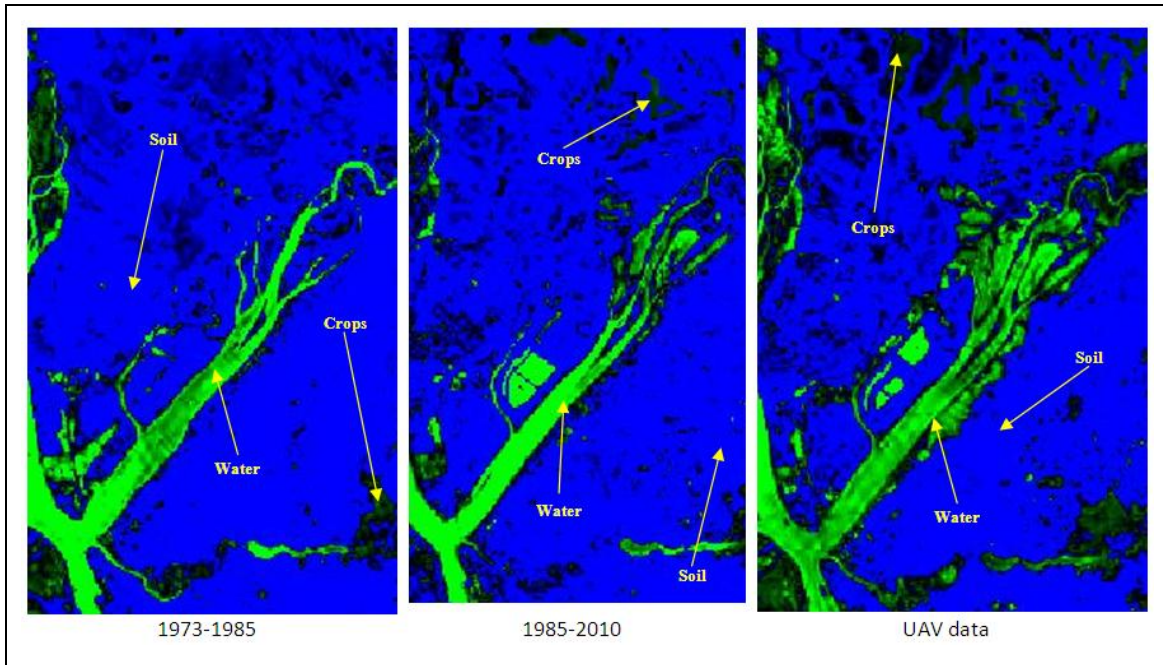


Figure 8: Image Classification During the Study Period

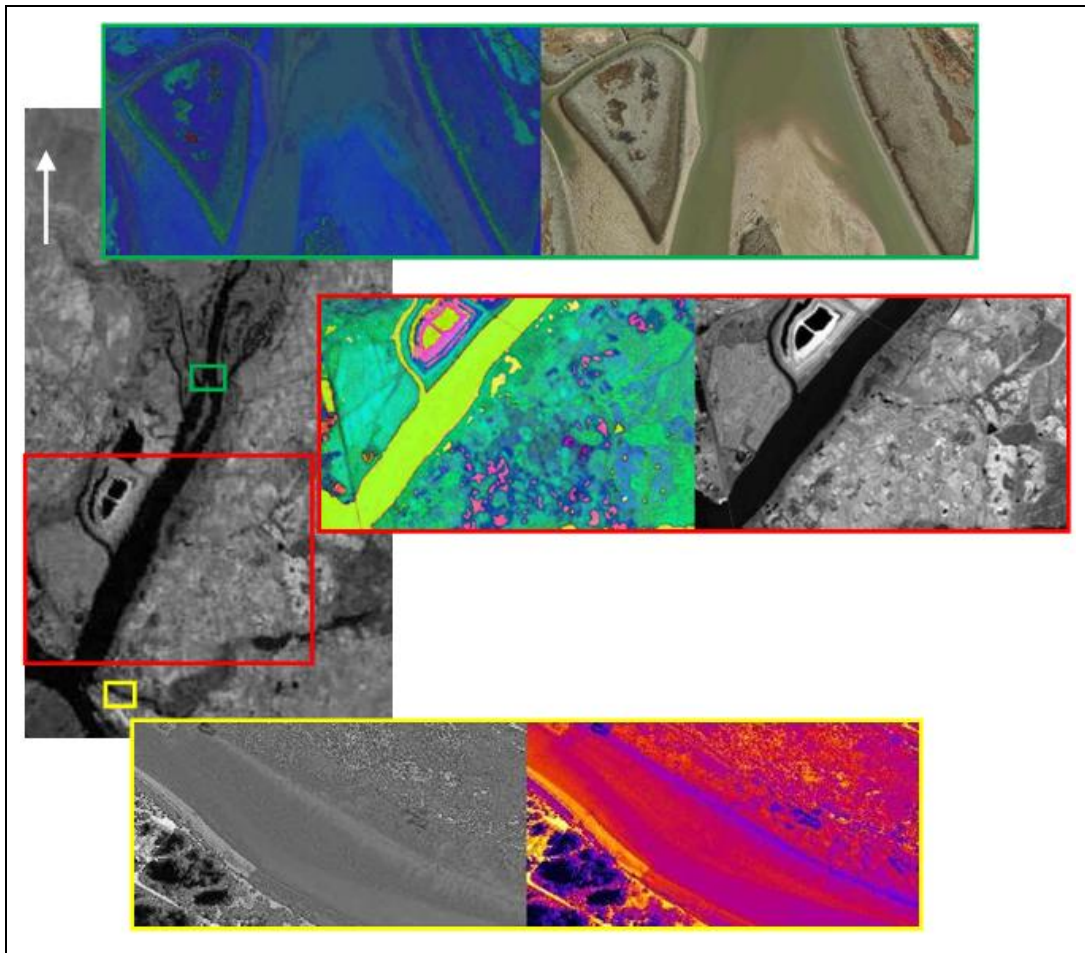


Figure 9: Image Classification in the Study Area

Erosion dynamic divides Tinto salt-marshes into two zones. The Southern zone presents the highest erosion rates due to tidal effects to a greater extent, with a mean value of total erosion of 0.19 m. Also, the higher levels of anthropogenic pressures (industrial activities among others) might contribute to increase the erosion [15]. However, in the Northern area, with a mean value of total erosion of 0.11 m, and with the existence of the Tartessos' Industrial Park, the dumping of raw sewage and solid waste increase the vulnerability of the area which can mask the real value of total erosion.

The erosion in the Tinto salt-marshes has caused, in the total of study period, a loss of 3,850,000 m<sup>2</sup> of equivalent area giving rise to a total volume of eroded soil of – 1,136,640 m<sup>3</sup>. According to [15], this erosion hinders the development of marshes by successional processes.

## 4 Conclusion

In the Tinto salt-marshes, Southwest of the Iberian Peninsula, the different causes that give rise to the erosion processes were investigated. The results, after analyzing the meteorological data, showed an annual filling process coinciding with the months of highest rainfall, and a water loss concentrated in the summer months. In this regard, the use of different DEMs gave rise to the prediction of volumes with significant differences between periods. One of the main factors of these significant differences is the ecological preservation of the study area in the middle of the second period (1985-2010). This is related to the gradual increase in temperature in recent years, and with the gradual decrease of rainfall (dry period), which together with the slow accumulation of sediments favors the loss of equivalent area in the total of the study period.

In turn, the LUC produced in Tinto salt-marshes is related to loss of wetlands and littoral water areas, not only because of the two processes that accelerate the conversion of forest stand in scrub areas or pastureland and therefore the change of typology within the LUC of forestry and natural areas, but also to the progressive increase of the negative rate of eroded soil (sediment deposition) that might also reflect lower energy, and therefore a possible rise in sea level, resulting in a decrease in the kinetic energy in the Tinto river [16].

Similar results were found in the prediction of the erosion processes using both photogrammetric and UAV images, so it necessary to emphasize the importance of using UAV's to study phenomena related to the environment, and its suitability in the study and evolution of LUC.

## REFERENCES

- [1]. Ian P. Prosser, Ian D. Rutherford, Jon M. Olley, William J. Young, Peter J. Wallbrink, and Chris J. Moran, *Large-Scale Patterns of Erosion and Sediment Transport in River Networks, with Examples from Australia*. Mar. Freshwater Res., 2001. 52: p. 81-99.
- [2]. Ramírez-Juidías, E., López-Lineros, M., and Madueño-Luna, A., *Predicción anual de los cambios volumétricos de las Marismas de Doñana mediante el uso de imágenes satélite*, in *Book Abstracts V Congreso Nacional y II Congreso Ibérico Agroingeniería*, Sociedad Española de Agroingeniería, Editor 2009. p. 199-200.

- [3]. Custodio, E., *Aguas subterráneas y humedales*, in *Proceeding Book VII Simposio de Hidrología*, Asociación Española de Hidrólogos, Editor 2001. p. 3-30.
- [4]. Joachim Hill, and Brigitta Schütt, *Mapping Complex Patterns of Erosion and Stability in Dry Mediterranean Ecosystems*. *Remote Sens. Environ.*, 2000. 74: p. 557-569.
- [5]. Ramírez-Juidías, E., Tejero-Manzanares, J., Moreno-Fresno, J.J., Justicia Segovia, M., Madueño Luna, A., and López-Lineros, M., *Land Use Changes and Volumetric processes in the Tinto Salt-Marshes*, in *Book Abstracts 3rd International Conference on Challenges in Environmental Science and Computer Engineering*, G. Lee, Editor 2014. p. 5-5.
- [6]. Ojeda-Zújar, J., and Márquez-Pérez, J., *Modelos Digitales de Elevaciones (MDE) para la Caracterización Altimétrica de Espacios Marismesños: Las Marismas del Odiel (Huelva)*. *Rev. Soc. Geol. España*, 1997. 10(1-2): p. 147-161.
- [7]. Juidías, E.R., Segovia, M.J., and Luna, A.M., *New Method to Predict the Volumetric Changes in the Odiel Marshes (Huelva, Spain)*. *Lecture Notes in Engineering and Computer Science: Proceeding of the World Congress on Engineering*, 2013, U.K., 3-5 July, 2013, London. p. 1335-1339.
- [8]. Castellanos, E.M., Nieva, F.J., Luque, C.J., and Figueroa, M.E., *Modelo Anual de la Dinámica Sedimentaria en una Marisma Mareal Mediterránea*. *Cuaternario y Geomorfología*, 1998. 12(3-4): p. 69-76.
- [9]. Henry, J.B., Matgen, P., Tholey, N., Pfister, L., Hoffmann, L., and De Fraipont, P., *Vers une Intégration des Techniques Spatiales pour la Gestion des Inondations*. *Bulletin de la Société Française de Photogrammétrie et de Télédétection*, 2003. 172: p. 99-106.
- [10]. Matgen, P., Schumann, G., Henry, J.B., Hoffmann, L., and Pfister, L., *Integration of SAR-Derived River Inundations Areas, High-Precision Topographic Data and a River Flow Model Toward Near Real-Time Flood Management*. *International Journal of Applied Earth Observation and Geoinformation*, 2007. 9: p. 247-263.
- [11]. Instituto de Estadística de Andalucía, *Entorno físico en Andalucía: estadísticas históricas del siglo XX*. 1st edition ed2007, Sevilla:Junta de Andalucía (Spain). 306.
- [12]. Consejería de Medio Ambiente, *Medio siglo de cambios en la evolución de usos del suelo en Andalucía 1956-2007*. 1st edition ed2011, Sevilla:Junta de Andalucía (Spain). 174.
- [13]. Lowry, R. *VassarStats: Website for Statistical Computation*, <http://vassarstats.net/anova1u.html>. 2001.
- [14]. Ramírez-Juidías, E., Pozo-Morales, L., and Galán-Ortiz, L., *Procedimiento para la Obtención de una Imagen Teledetectada a Partir de Fotografía*. 14/06/2013. Universidad de Sevilla, Spain, Patent nº P201300573 (with extension to International Patent W2014000097).
- [15]. Castillo, J.M., Rubio-Casal, A.E., Luque, C.J., Nieva, F.J., and Figueroa, M.E., *Wetland Loss by Erosion in Odiel Marshes (SW Spain)*. *Journal of Coastal Research*, 2002. 36: p. 134-138.
- [16]. Rogers, C.E., and McCarty, J.P., *Climate Change and Ecosystems of the Mid-Atlantic Region*. *Climate Research*, 2000. 14(3): p. 235-244.

# A New Comparative Study of Radiometric Correction on Satellite Images Using Kalman Filter and Levenberg Marquardt Algorithm

**Priti Tyagi, Udhav Bhosle**

*PVPP College of Engineering, Rajiv Gandhi Institute of Technology, India*  
tpriti15@rediffmail.com, udhavgbhosle@gmail.com

## ABSTRACT

With the development of satellite and remote sensing techniques, more and more multi-temporal image data from airborne/satellite sensors have been collected and used in huge amounts to monitor the changes in land use and land cover. Radiometric consistency among collected multi-temporal imagery is difficult to maintain, because of variations in sensor characteristics, atmospheric conditions, solar angle, and sensor view angle. Radiometric corrections are used to remove the effects that alter the spectral characteristics of land features, except for actual changes in ground target, becoming mandatory in multi-sensor, multi-date studies. In this paper, a comparative analysis of radiometric correction of satellite images is made between Kalman filter and Levenberg algorithm. In first phase, the satellite images such as Landsat, Liss-3 have been corrected using Kalman filter technique. In the second phase, by using Levenberg algorithm radiometric correction has been performed. After that comparative study is made between the results of both techniques using different performance measures such as completeness, correctness and quality.

**Keywords:** Satellite Image, Radiometric Correction, Kalman Filter, Levenberg Algorithm, prediction.

## 1 Introduction

Nowadays satellite and airborne remote sensing system provides an enormous amount of data which are invaluable in monitoring Earth resources and the effects of human activities [2] [3] and [4]. Remote sensing is used to analyze the information about a target or an area or a phenomenon that are obtained through the remote sensor [5]. One of the advantages of remote sensing is that the measurements can be made from a large distance of about several hundred to thousand kilometers, which means that large areas on ground can be covered easily [6].

Satellite remote sensing data can provide a complement or even alternative to ground-based research for large scale studies or over long periods and is an invaluable tool for scientists, governments and the military [7] [8]. Images obtained by satellites are widely used in many environmental applications such as tracking of earth resources, geographical mapping, prediction of agricultural crops, urban growth, weather, flood and fire control etc. Space image application includes recognition and analysis of objects in the images, obtained from deep space-probe missions [9].

Satellite imaging systems like Landsat, Ikonos, QuickBird, OrbView-3, etc. has been used to collect and downlink large quantities of data [6, 8, and 9]. Images obtained through these satellites are subjected to several factors such as launch shock, loss of moisture due to vacuum, and gravity release, which will cause the values of the geometric calibration parameters to vary between the time of ground calibration and on-orbit operation [12]. Satellite image characteristics vary from date to date [8], and radiometric inconsistency among ground targets in multi-temporal imagery is produced due to the changes in sensor characteristics, atmospheric condition, solar angle, and sensor view angle [14]. Additional variation is caused by atmospheric conditions at the time of imaging, due to haze the image can be scattered at different wavelengths [8].

Therefore, radiometric corrections are performed on the raw digital image data to correct for brightness values, of the object on the ground, that have been distorted because of sensor calibration or sensor malfunction problems [13]. Radiometric corrections are classified into two types; they are absolute correction and relative corrections. Absolute radiometric correction is used to extract the absolute reflectance of scene targets at the surface of the earth and relative radiometric correction is used to reduce atmospheric and other unexpected variation among multiple images by adjusting the radiometric properties of target images to match a base image [14].

The structure of the paper is organized as follows: A brief review of the researches related to the radiometric correction is given in Section 2. The proposed comparative study of radiometric correction technique on satellite images is given in section 3. The experimental results of the proposed approach are presented in Section 4. Finally, the conclusions are given in Section 5.

## 2 Related Work

Some of the recent research works on radiometric correction of satellite images are briefly reviewed here.

In 2006, Leonardo Paolini *et al.*, [15] have discussed the effects of two types of radiometric correction methods (absolute and relative) for the determination of land cover changes, using Landsat TM and Landsat ETM+ images. In addition, they have presented an improvement to

make the relative correction method addressed. Absolute correction include a cross calibration between TM and ETM+ images, and the application of an atmospheric correction protocol. Relative correction was used to normalize the images using pseudo-invariant features (PIFs) selected through band-to-band PCA analysis. They have used an algorithm for PIFs selection, in order to improve normalization results. A post-correction evaluation index (Quadratic Difference Index (QD)), and post-classification and change detection results were used to evaluate the performance of their method. Their method has shown good post correction and post-classification results for all the images have been used (QD index < 0; overall accuracy .80%; kappa .0.65).

In 2006, Todd A. Schroeder *et al.*, [16] have presented a comparison of five atmospheric correction methods (2 relative, 3 absolute) used to correct a nearly continuous 20-year Landsat TM/ETM+ image data set (19-images) covering western Oregon (path/row 46/29). In theory, full absolute correction of individual images in a time-series have minimized the atmospheric effects resulted in a series of images that appeared more similar in spectral response than the same set of uncorrected images. To contradict that theory, they have demonstrated absolute correction methods such as Second Simulation of the Satellite Signal in the Solar Spectrum (6 s), Modified Dense Dark Vegetation (MDDV), and Dark Object Subtraction (DOS). The relative methods were the variants of an approach called absolute-normalization. This method was used to match the images in a time-series to an atmospherically corrected reference image using pseudo-invariant features and reduced major axis (RMA) regression. An advantage of “absolute-normalization” was that all images in the time-series were converted to units of surface reflectance while simultaneously being corrected for atmospheric effects. Of the two relative correction methods used for “absolute-normalization”, the first employed an automated ordination algorithm called multivariate alteration detection (MAD) to statistically locate pseudo-invariant pixels between each subject and reference image, while the second used analyst selected pseudo-invariant features (PIF) common to the entire image set. Overall, relative correction has been employed in the “absolute-normalization” context to produce the most consistent temporal reflectance response, with the automated MAD algorithm and handpicked PIFs. The “absolute normalization” scheme has improved (i.e., reduces scatter in) the spectral reflectance trajectory models used for characterizing patterns of early forest succession.

In 2008, Mahmoud El Hajj *et al.*, [17] have discussed the relative radiometric normalization for atmospheric correction. They have developed an automatic method for relative radiometric normalization based on calculating linear regressions between un-normalized and reference images. Regressions were obtained using the reflectance of automatically selected invariant targets. They have compared their method with a 6S model based atmospheric correction method. The performances of both methods were compared using 18 images from of a SPOT 5 time series acquired over Reunion Island. The results obtained for a set of manually selected invariant targets showed an excellent agreement between the two methods in all spectral

bands: values of the coefficient of determination ( $r^2$ ) exceed 0.960, and bias magnitude values were less than 2.65. Also there have been a strong correlation between normalized NDVI values of sugarcane fields ( $r^2 = 0.959$ ). Despite a relative error of 12.66% between values, very comparable NDVI patterns were observed.

In 2009, Wadii Boulila *et al.*, [7] have discussed the problem of tracking spatiotemporal changes of a satellite image through the use of Knowledge Discovery in Database (KDD). They have used prediction and decision models to discover the interesting knowledge of a given user effectively. The main objective of their work was using different KDD methods to discover knowledge in satellite image databases. Each method presented a different point of view of spatiotemporal evolution of a query model (which represents an extracted object from a satellite image). In order to combine those methods, they have used the evidence fusion theory to improve the spatiotemporal knowledge discovery process and increase the spatiotemporal model change. The experimental results of satellite images represented the region of Auckland in New Zealand depict the improvement in the overall change detection when compared to using classical methods.

In 2010, Andrea Baraldi *et al.*, [18] have analyzed the operational performance of existing stratified non-Lambertian (anisotropic) topographic correction (SNLTOC) algorithms which had been limited by the need for a priori knowledge of structural landscape characteristics, such as surface roughness. To overcome the circular nature of the SNLTOC problem, a mutually exclusive and totally exhaustive land covers classification map of a space borne MS image was required before SNLTOC takes place. Thus in their work, two methods were cascaded such as an automatic stratification at first stage and a second-stage ordinary SNLTOC method. The former has combined four sub symbolic digital-elevation-model-derived strata, namely, horizontal areas, self-shadows, and sunlit slopes either facing the sun or facing away from the sun, and 2) symbolic (semantic) strata generated from the input MS image by an operational fully automated spectral-rule-based decision-tree preliminary classifier. In this work, previous works related to the TOC subject were surveyed, and next, the operational two-stage SNLTOC system was presented. Finally, the original two-stage SNLTOC system was validated up to 19 experiments where the system's capability of reducing within-stratum spectral variance while preserving pixel-based spectral patterns (shapes) was assessed quantitatively.

In 2011, Priti Tyagi *et al.*, [1] presented eight methods for atmospheric correction in spatial domain and transform domain. They proposed atmospheric correction using linear regression model based on the wavelet transform and fourier transform. They were tested on landsat images and their performance was evaluated using visual and statistical measures. The application of the atmospheric correction methods for vegetation analyses using NDVI was also presented in the paper. Atmospheric correction using Radon Regression was also presented by the author [22] for radiometric correction of multispectral Image.

### 3 Radiometric Correction By Means of Kalman Filter and Levenberg Algorithm

Over the last few years, the satellite image analysis has played a significant role in environmental monitoring and modeling. Frequent observation of a given area over time yields the potential for several forms of change detection analysis. This radiometric inconsistency is formed due to the changes in sensor calibration, differences in illumination and observation angles, and variation in atmospheric effects [Janzen et al]. This type of deformity in satellite images should be corrected to allow for metric analyses and also adjustments may need to be applied to correct the non-homogeneous contrasts and tonal differences between adjacent frames. Thus in our research work, we have performed the radiometric correction on aerial images using two efficient methods. The proposed technique carries out in two phases. In the first phase kalman filter is applied to the remotely sensed data for obtaining predict and update state values of noisy image. In the second phase the radiometric correction on satellite images can be obtained by using Levenberg algorithm. Finally a comparison performed between corrected images resulting from both techniques. The flow diagram of the proposed scheme is given below:

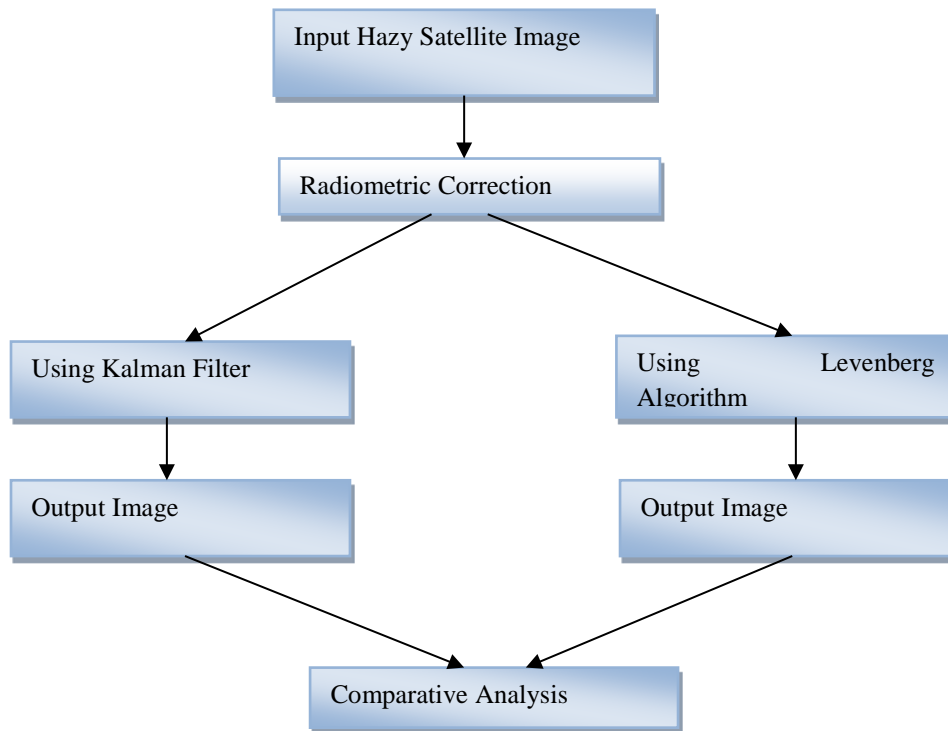


Fig 1: Flow Diagram of the proposed method

#### 3.1 Radiometric Correction Using Kalman Filter:

In 1960, Kalman filter concept has been introduced by R.E. Kalman to find the recursive solution for the discrete-data linear filtering problem. The Kalman filter is a set of mathematical equations, which offers an efficient computational (recursive) way to calculate the state of a

process, in a way that reduces the mean squared error. The filter is utilized to support the estimation of past, present, and even future states, when the precise nature of the modeled system is unknown. The Kalman filter algorithm has been implemented by two-step process, named as prediction step and update step. In the prediction stage, the Kalman filter produces estimates of the present state variables, along with their uncertainties. In the update stage, when the result of the next measurement (inevitably corrupted with some amount of error, including random noise) is observed, those estimates are updated by a weighted average, with more weight being given to estimates with higher certainty.

In steady state, the Kalman approach to radiometric correction of satellite images is depicted by the following equations,

$$x_k = Ax_{k-1} + w_{k-1} \quad (1)$$

Where,  $x_k$  is the current state vector, which contains set of variables to represent the whole system at time instant  $k$ . Also the value of  $x_k$  depends on the state transition model  $A$  applied to previous state value  $x_{k-1}$  and previous state noise  $w_{k-1}$ .

The measurement vector  $y_k$  according to the current state vector  $x_k$  applied to measurement model  $B$  and the measurement noise  $z_k$  is given as,

$$y_k = Bx_k + z_k \quad (2)$$

The random variables of state noise and measurement noise are represented as  $\{w_k\}$ ,  $\{z_k\}$  and also the error covariance of state noise and measurement noise is given in equation (3)

$$\begin{aligned} E[w_k w_l] &= Q_{kl} & p(w_k) &\sim N(0, Q) \\ E[z_k z_l] &= R_{kl} & p(z_k) &\sim N(0, R) \end{aligned} \quad (3)$$

### 3.1.1 Prediction

The Kalman filter estimates the state at time instant  $k$  and subsequently, it obtains the feedbacks in terms of noisy measurements.

Predicted (a priori) state estimate is,

$$\hat{x}_{k/k-1} = A\hat{x}_{k-1/k-1} \quad (4)$$

Predicted (a priori) estimate covariance is,

$$P_{k/k-1} = AP_{k-1/k-1}A^T + Q \quad (5)$$

### 3.1.2 Updating

Kalman gain is given as,

$$K_k = P_{k/k-1} B_k^T [D_k]^{-1} \tag{6}$$

Where,  $D_k = B_k P_{k/k-1} B_k^T + R$

Updated (a posteriori) state estimate and updated (a posteriori) estimate covariance is given in the following equations:

$$\hat{x}_{k/k} = \hat{x}_{k/k-1} + K_k (y_k - B_k \hat{x}_{k/k-1}) \tag{7}$$

$$P_{k/k} = [I - K_k B_k] P_{k/k-1} \tag{8}$$

### 3.2 Radiometric correction using Levenberg Marquardt (LM) Algorithm:

The Levenberg-Marquardt (LM) algorithm is the most extensively utilized optimization algorithm [20]. It outperforms simple gradient descent and other conjugate gradient methods in a wide variety of problems. It is the most prominent curve-fitting algorithm used in numerous software applications for solving generic curve-fitting problems. Here, the problem is the radiometric inconsistency of the satellite images. Given a set of  $n$  data pairs of independent and dependent variables  $(x_i, y_i)$ , and optimize the parameters  $\beta$  of the model curve so that, the minimal function  $R(\beta)$  is given as,

$$R(\beta) = \sum_{i=1}^n [y_i - f(x_i, \beta)]^2 \tag{9}$$

Steps involved in Levenberg Marquardt (LM) Algorithm:

(i) To begin the iterative procedure of the Levenberg Marquardt algorithm for minimization, the user has to assume the value for parameter vector  $\beta$ .

(ii) In each iteration, the parameter vector  $\beta$  is replaced by a new estimate  $\beta + \delta$

(iii) To find  $\delta$ , the functions  $f(x_i, \beta + \delta)$  are approximated by their linearizations  $f(x_i, \beta + \delta) \approx f(x_i, \beta) + J_i \delta$

Where  $J_i$  is the gradient of  $f$  with respect to  $\beta$  and is given by,  $J_i = \frac{\partial f(x_i, \beta)}{\partial \beta}$

(iv) To determine the minimum of the sum of squares  $R(\beta)$ , the gradient of  $R$  with respect to  $\delta$  will be zero. The above first-order approximation of  $f(x_i, \beta + \delta)$  is given as,

$$R(\beta + \delta) \approx \sum_{i=1}^n (y_i - f(x_i, \beta) - J_i \delta)^2 \tag{10}$$

(v) Taking the derivative with respect to  $\delta$  and setting the result to zero gives

$$(J^T J) \delta = J^T [y - f(\beta)] \tag{11}$$

Where  $J$  is the Jacobian matrix,  $y$  and  $f$  are the vectors containing elements  $y_i$ ,  $f(x_i, \beta)$  respectively.

(vi) By Levenberg's contribution, the above equation is replaced by a "damped version", which is represented as,

$$(J^T J + \lambda I) \delta = J^T [y - f(\beta)] \quad (12)$$

Where  $I$  is the Identity matrix, giving as the increment  $\delta$  to the parameter vector  $\beta$  and the non negative factor  $\lambda$  is adjusted for each iteration.

(vii) The drawback of Levenberg's algorithm is, if the value of damping factor  $\lambda$  is large, then inverting  $J^T J + \lambda I$  becomes tricky. Thus Marquardt replaced the identity matrix  $I$  with the diagonal matrix consisting of the diagonal elements  $J^T J$ . Thus the resulting Levenberg–Marquardt algorithm is,

$$(J^T J + \lambda \text{diag}(J^T J)) \delta = J^T [y - f(\beta)] \quad (13)$$

## 4 Experimental Data and Results

The proposed comparative study of radiometric correction using both techniques was done in the working platform of MATLAB.

### 4.1 Experimental Data:

The satellite images used in the proposed work are obtained from LISS-III and Landsat 7 ETM+ sensors which are given in Fig 2. A LISS-III satellite image acquired in March 2, 2006 is shown in fig 2(a) and a Landsat 7 ETM+ image acquired in March 2000 to show the region of San Francisco is shown in fig 2(b). The sensor specifications such as band type, resolution, wavelength and description of each band of input Landsat 7 ETM+ image is detailed in Table 1.

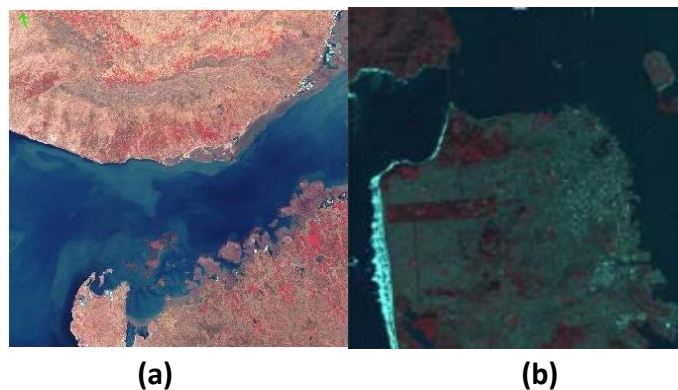


Fig 2: Input Images, a) LISS-III satellite image, b) Landsat ETM+ satellite image

**Table 1: Landsat ETM+ sensor specifications**

Band	Resolution( <i>m</i> )	Wavelength( $\mu m$ )	Description
1	30m	0.45-0.52	Blue
2	30m	0.52-0.60	Green
3	30m	0.63-0.69	Red
4	30m	0.76-0.90	Near Infrared
5	30m	1.55-1.75	Short-wave Infrared
6	60m	10.4-12.5	Thermal Infrared
7	30m	2.09-2.35	Short-wave Infrared
8	15m	0.45-0.80	Panchromatic

## 4.2 Results and Analysis:

The experiments have been conducted on the input LISS-III and Landsat 7 ETM+ satellite images using Kalman filter and Levenberg-Marquardt (LM) algorithm. Fig 3 illustrates the resultant of both satellite images obtained using Kalman filter and Fig 4 shows the output images obtained by using Levenberg-Marquardt (LM) algorithm.



**Fig 3: Radiometric corrected output using Kalman filter for (a) LISS-III satellite image (b) Landsat 7 ETM+ satellite image.**



(a) (b)

**Fig 4: Radiometric corrected output using Levenberg-Marquardt (LM) algorithm for (a) LISS-III satellite image (b) Landsat 7 ETM+ satellite image.**

Our proposed method improves the quality of remote sensing data by means of Kalman filter and Levenberg-Marquardt (LM) algorithm. Different quality measures such as Peak Signal to Noise Ratio, Mean Square Error and Root Mean Square Error has been calculated for both methods and is given in Table 2, and 3.

As per Table 2, by using the Kalman filter for radiometric correction on LISS-III satellite image, obtained PSNR, MSE and RMSE values are +27.73091 dB, 331.52031 and 18.20770 respectively. While using the same filter for Landsat image, PSNR, MSE and RMSE values are +31.85306 dB, 128.32016 and 11.32785 respectively. Table 3 illustrates the quality measurements (PSNR, MSE, and RMSE) of both satellite images using Levenberg-Marquardt (LM) algorithm. For LISS-III image, PSNR, MSE and RMSE values are +17.86615 dB, 3213.55751 and 56.6882. For Landsat image, PSNR, MSE and RMSE values are +27.22954 dB, 372.08957 and 19.28962 respectively. Table 4 illustrates the comparison results of Kalman filter and Levenberg-Marquardt (LM) algorithm for LISS-III and Landsat 7 ETM+ satellite images respectively.

**Table 2: Quality Metrics of LISS-III and Landsat ETM+ satellite images Using Kalman filter**

Quality Metrics	LISS-III satellite Image	Landsat 7 ETM+ satellite Image
PSNR	+27.73091 dB	+31.85306 dB
MSE	331.52031	128.32016
RMSE	18.20770	11.32785

**Table 3: Quality Metrics of LISS-III and Landsat ETM+ satellite images Using Levenberg-Marquardt (LM) algorithm**

Quality Metrics	LISS-III satellite Image	Landsat 7 ETM+ satellite Image
PSNR	+17.86615 dB	+27.22954 dB
MSE	3213.55751	372.08957

RMSE	56.6882	19.28962
------	---------	----------

Table 4: Quality Metrics Comparison Results

Quality Metrics	LISS-III satellite Image		Landsat 7 ETM+ satellite Image	
	Kalman filter	Levenberg-Marquardt	Kalman filter	Levenberg-Marquardt
PSNR	+27.73091 dB	+17.86615 dB	+31.85306 dB	+27.22954 dB
MSE	331.52031	3213.55751	128.32016	372.08957
RMSE	18.20770	56.6882	11.32785	19.28962

From the values represented in Table 4, it can be seen that for LISS-III satellite image, the PSNR value of Kalman filter output is higher than Levenberg-Marquardt output. According to the MSE and RMSE values, the Kalman filter output is low when compared to the Levenberg-Marquardt algorithm output. Also, for Landsat 7 ETM+ satellite image the PSNR value of Kalman filter output is greater than Levenberg-Marquardt method. The MSE and RMSE values of Kalman filter output is relatively low when compared with the Levenberg-Marquardt algorithm output. By comparing PSNR, MSE and RMSE values from the above table, it is shown that the radiometric correction performance of Kalman filter is relatively high for both types of satellite images.

## 5 Conclusion

In this paper, comparative analysis of radiometric correction on different types of satellite images was made using two efficient techniques such as Kalman filter and Levenberg-Marquardt algorithm. First of all, Kalman filter has been utilized for radiometric correction on remote sensing data and after that Levenberg-Marquardt algorithm has been used for the same process. The study helped to analyze the performance of both methods for radiometric correction on different satellite images by means quality parameters such as peak signal to noise ratio, mean square error and root mean square error. From the experimental results, we can conclude that Kalman filter works in a better way to perform the radiometric correction on different satellite images.

## REFERENCES

- [1] Priti Tyagi, Udhav Bhosle, "Atmospheric correction of Remotely sensed Images in Spatial and Transform Domain", International Journal of Image Processing, Vol(5), Issue (5), pp 564-579, 2011

- [2] Seema Biday, and Udhav Bhosle, "Relative Radiometric Correction of Cloudy Multitemporal Satellite Imagery", *International Journal of Civil and Environmental Engineering*, Vol.2, No.3, 2010.
- [3] Mirnalinee Dhinesh, Sukhendu Das and Koshy Varghese, "Automatic Curvilinear Structure detection from Satellite Images using Multiresolution GMM ", *International Journal of Imaging Science and Engineering (IJISE)*, Vol.2, No.1, pp. 154-157, 2008.
- [4] Michael Schroder, Hubert Rehrauer, Klaus Seidel, and Mihai Datcu, "Spatial Information Retrieval from Remote-Sensing Images—Part II: Gibbs–Markov Random Fields", *IEEE Transactions on geoscience and remote sensing*, Vol. 36, No. 5, pp.1446-1455, 1998.
- [5] T Rajani Mangala and S G Bhirud, "An Effective ANN-Based Classification System for Rural Road Extraction in Satellite Imagery", *European Journal of Scientific Research*, Vol.47, No.4, pp.574-585, 2010.
- [6] Rajiv Kumar Nath and S K Deb, "Water-Body Area Extraction from High Resolution Satellite Images-An Introduction, Review, and Comparison", *International Journal of Image Processing (IJIP)*, Vol. 3, No.6, pp.353-372, 2010.
- [7] Wadii Boulila, Imed Riadh Farah, Karim Saheb Etabaa, Basel Solaiman, and Henda Ben Ghezala, "Improving Spatiotemporal Change Detection: A High Level Fusion Approach for Discovering Uncertain Knowledge from Satellite Image Databases", *World Academy of Science, Engineering and Technology*, Vol. 52, No.12, pp 52-57, 2009.
- [8] Sarah C. Goslee, "Analyzing Remote Sensing Data in R: The landsat Package", *Journal of Statistical Software*, Vol. 43, No.4, pp.1-25, 2011.
- [9] Salem Saleh Al-amri, N.V. Kalyankar and Khamitkar S.D, "A Comparative Study of Removal Noise from Remote Sensing Image", *IJCSI International Journal of Computer Science Issues*, Vol. 7, No. 1, pp. 32-36, 2010.
- [10] Ellison, J. and Milstein, J, "Improved Reduced-Resolution Satellite Imagery", In proceedings of Goddard Conf. on Space Applications of Artificial Intelligence & Emerging Info. Technologies in Los Angeles, CA, 9-11 May 1995, pp. 163-178.
- [11] H. Liu, J. Li and M. A. Chapman, "Automated Road Extraction from Satellite Imagery Using Hybrid Genetic Algorithms and Cluster Analysis", *Journal of Environmental Informatics*, Vol.1, No.2, pp.40-47, 2003.
- [12] David Mulawa, "On-Orbit Geometric Calibration Of The Orbview-3 High Resolution Imaging Satellite", In proceedings of the XXth International Society for Photogrammetry and Remote Sensing Congress (ISPRS), 2004.
- [13] S.Santhosh Baboo and M.Renuka Devi, "Geometric Correction in Recent High Resolution Satellite Imagery: A Case Study in Coimbatore, Tamil Nadu", *International Journal of Computer Applications*, Vol. 14, No.1, pp.32-37, 2011.

- [14] Xuexia Chena, Lee Vierlinga, and Don Deering, "A simple and effective radiometric correction method to improve landscape change detection across sensors and across time", *Remote Sensing of Environment Journal*, Vol. 98, No.1, pp.63–79, 2005.
- [15] Leonardo Paolini, Francisco Grings, Jose A. Sobrino, Juan C. Jime Nez Munoz and Haydee karszenbaum, "Radiometric correction effects in Landsat multi-date/multi-sensor change detection studies", *International Journal of Remote Sensing*, Vol. 27, No.4, pp.685–704, 2006.
- [16] T Schroeder, W Cohen, C Song, M Canty, and Z Yang, "Radiometric correction of multi-temporal Landsat data for characterization of early successional forest patterns in western Oregon", *Remote Sensing of Environment Journal*, Vol.103, No.1, pp. 685–704, 2006.
- [17] M. El Hajj , A. Begue , B. Lafrance , O. Hagolle , G. Dedieu , and M. Rumeau, "Relative radiometric normalization and atmospheric correction of a SPOT 5 time series", *Sensors Journal*, Vol.8, pp.2774 – 2791, 2008.
- [18] Andrea Baraldi, Matteo Gironda, and Dario Simonetti, "Operational Two-Stage Stratified Topographic Correction of Spaceborne Multispectral Imagery Employing an Automatic Spectral-Rule-Based Decision-Tree Preliminary Classifier", *IEEE transactions on geoscience and remote sensing*, Vol. 48, No. 1, pp.112-146, 2010.
- [19] Darren T. Janzen, Arthur L. Fredeen, and Roger D. Wheate, "Radiometric correction techniques and accuracy assessment for Landsat TM data in remote forested regions", *Can. J. Remote Sensing*, Vol. 32, No. 5, pp. 330–340, 2006.
- [20] R. E. Kalman, "A New Approach to Linear Filtering and Prediction Problems", *Journal of Basic Engineering*, Vol.82 (Series D), pp.35-45, 1960.
- [21] K. Levenberg, "A method for the solution of certain non-linear problems in least squares", *Quarterly Journal of Applied Mathematics*, Vol. II, No.22, pp.164--168,1944.
- [22] Priti Tyagi, Udhav Bhosle,"Radiometric correction of Multispectral Images using Radon Transform", *Journal of Indian Society of Remote Sensing*, DOI 10.1007/s12524-013-0307-y, 2013